Cell Reports

Resource

Polyamine metabolism dysregulation contributes to muscle fiber vulnerability in ALS

Graphical abstract

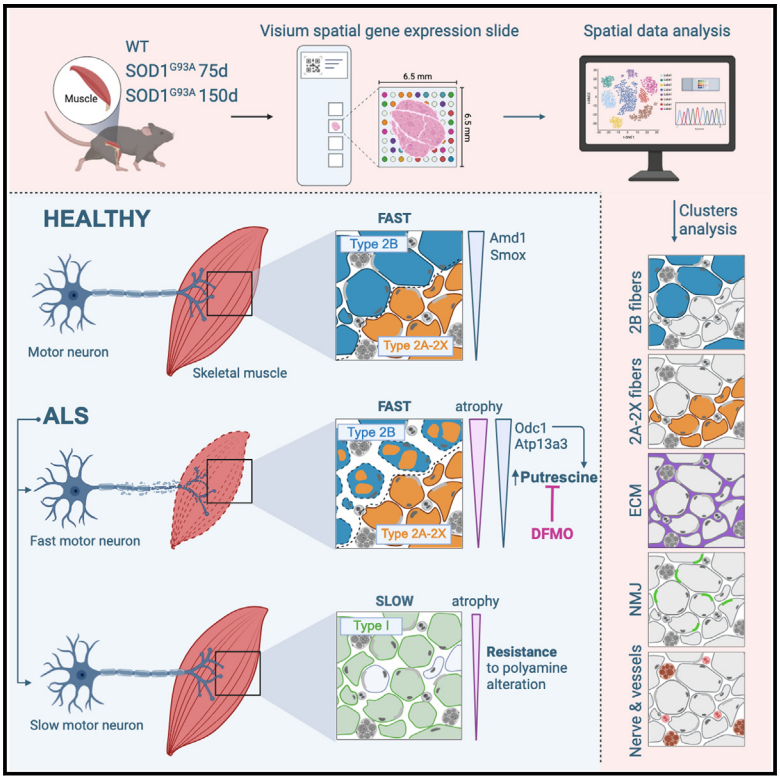

Highlights

- Spatial transcriptomics reveals distinct vulnerabilities among muscle fibers in ALS
- Muscle fiber defects are associated with disruptions in polyamine metabolism
- AMD1 inhibition leads to skeletal muscle impairment
- Restoring polyamine balance enhances muscle phenotype in ALS-affected mice

Authors

Veronica Ruggieri, Silvia Scaricamazza, Andrea Bracaglia, ..., Alberto Ferri, Lorenzo Giordani, Luca Madaro

Correspondence

lorenzo.giordani@sorbonne-universite.fr (L.G.),
luca.madaro@uniroma1.it (L.M.)

In brief

Ruggieri et al. developed a spatial transcriptomics dataset of skeletal muscle from the SOD1^{G93A} ALS mouse model. Their findings highlight polyamine metabolism's role in muscle fiber vulnerability, showing that disruptions of this metabolic pathway cause muscle defects, while restoring polyamine balance improves muscle function in diseased mice.

Ruggieri et al., 2025, Cell Reports *44*, 115123
January 28, 2025
https://doi.org/10.1016/j.celrep.2024.115123

CellPress

Cell Reports

CellPress
OPEN ACCESS

Resource

Polyamine metabolism dysregulation contributes to muscle fiber vulnerability in ALS

Veronica Ruggieri,[1,2] Silvia Scaricamazza,[3,4] Andrea Bracaglia,[1,2] Chiara D'Ercole,[1,5] Cristina Parisi,[1,2] Paolo D'Angelo,[1,2] Daisy Proietti,[6] Chiara Cappelletti,[7] Alberto Macone,[7] Biliana Lozanoska-Ochser,[8] Marina Bouchè,[1] Lucia Latella,[4] Cristiana Valle,[3,4] Alberto Ferri,[3,4] Lorenzo Giordani,[5,*] and Luca Madaro[1,2,9,*]

[1]Department of Anatomical, Histological, Forensic Sciences and Orthopedics, Sapienza University of Rome, 00161 Rome, Italy
[2]Laboratory affiliated with Istituto Pasteur Italia-Fondazione Cenci Bolognetti, 00161 Rome, Italy
[3]Laboratories of Neurochemistry and of Molecular and Cellular Neurobiology, IRCCS, Fondazione Santa Lucia, 00143 Rome, Italy
[4]National Research Council (CNR), Institute of Translational Pharmacology (IFT), 00133 Rome, Italy
[5]Sorbonne Université, INSERM UMRS 974, Association Institut de Myologie, Centre de Recherche en Myologie, 75013 Paris, France
[6]Cell Therapy for Myopathies Unit, Division of Neurosciences, San Raffaele Hospital, 20132 Milano, Italy
[7]Department of Biochemical Sciences, Sapienza University of Rome, 00185 Rome, Italy
[8]Department of Medicine & Surgery LUM University, 70010 Casamassima, Italy
[9]Lead contact
*Correspondence: lorenzo.giordani@sorbonne-universite.fr (L.G.), luca.madaro@uniroma1.it (L.M.)
https://doi.org/10.1016/j.celrep.2024.115123

SUMMARY

Amyotrophic lateral sclerosis (ALS) is a fatal neurodegenerative disease causing progressive paralysis due to motor neuron degeneration with no curative therapy despite extensive biomedical research. One of the primary targets of ALS is skeletal muscle, which undergoes profound functional changes as the disease progresses. To better understand how altered innervation interferes with muscle homeostasis during disease progression, we generated a spatial transcriptomics dataset of skeletal muscle in the SOD1^{G93A} mouse model of ALS. Using this strategy, we identified polyamine metabolism as one of the main altered pathways in affected muscle fibers. By establishing a correlation between the vulnerability of muscle fibers and the dysregulation of this metabolic pathway, we show that disrupting polyamine homeostasis causes impairments similar to those seen in ALS muscle. Finally, we show that restoration of polyamine homeostasis rescues the muscle phenotype in SOD1^{G93A} mice, opening new perspectives for the treatment of ALS.

INTRODUCTION

Amyotrophic lateral sclerosis (ALS) is a fast-progressing neurodegenerative disease characterized by degeneration of motor neurons (MNs) leading to paralysis and death within 2–3 years of onset.[1]

ALS is a highly heterogeneous disease with sporadic (sALS) and familial (fALS) cases.[2] Although the precise etiology of ALS remains elusive, many genetic factors related to RNA metabolism, oxidative stress, and protein homeostasis have been described.[1,2] Indeed, ALS-associated genes play a role in mitochondrial and mitochondrion-associated functions; these include superoxide dismutase 1 (SOD1), which is mutated in 10%–20% of fALS cases.[3] Due to lack of effective drugs, there is an urgent need for new treatment modalities for ALS. In this context, it is crucial to understand the contribution of different tissues involved in ALS progression. It is now widely accepted that neuromuscular junction (NMJ) disassembly and the resulting skeletal muscle denervation are critical pathogenic events in disease advancement.[4–9] In the early stages of the disease, skeletal muscle alterations have been linked to MN death and metabolic dysfunction.[7,10–18] These studies have provided strong evidence that skeletal muscle plays a critical role in the etiology of ALS, and as such, should be considered as an important therapeutic target. In this regard, understanding why certain muscle fiber types are more resistant to the disease could facilitate the identification of new therapeutic targets. It is now clear that slow muscles with oxidative metabolism, primarily composed of slow-twitch fibers (type 1), are more resistant than fast muscles with glycolytic metabolism, which are composed of fast-twitch fibers (type 2B, type 2X, and type 2A).[4,19] Indeed, there is a gradient of vulnerability in both MNs and muscles, where faster motor units are affected before slower ones, resulting in muscle atrophy that affects fast muscles earlier compared to slow ones.[20–24]

The emergence of innovative technologies capable of spatially analyzing gene expression may hold the key to a better understanding of how, within the same muscle, different fiber classes are involved in disease progression.[25–33] Using these methods, we generated a spatial transcriptomics (ST) dataset of the skeletal muscle in a mouse model of ALS during disease progression. Our approach identified a close correlation between muscular atrophy, energy metabolism, and regulation of polyamines in muscle fibers.

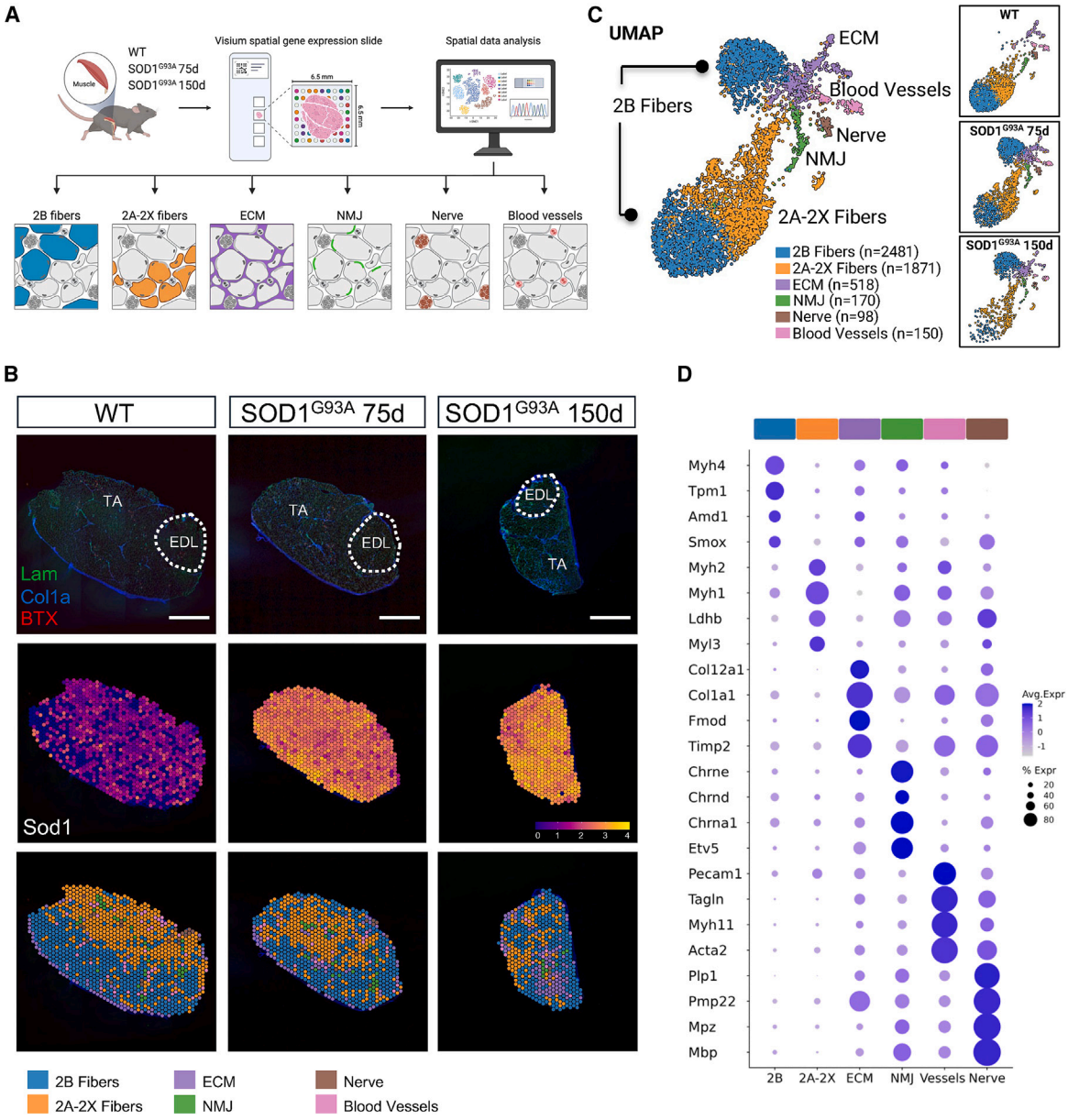

Figure 1. ST gene expression clustering of SOD1^{G93A} muscle

(A) Diagram of the experimental procedure for spatial transcriptomics (ST) on SOD1^{G93A} muscles using the 10× Visium platform.

(B) Immunofluorescence staining (top) for laminin (green) and collagen 1 (blue) on TA and EDL muscle cryosections, used for ST analysis, of WT and SOD1^{G93A} mice at 75 and 150 days of age; NMJs were stained with fluorescent alpha-bungarotoxin (BTX) (red) (scale bar, 1 mm). Shown are relative expression levels of the Sod1 gene (center) throughout the tissue during ALS progression and clusters identified by ST analysis on WT and SOD1^{G93A} muscle sections (bottom). The Visium array spots are color coded according to the cluster assignment of the combined dataset.

(C) Uniform manifold approximation and projection (UMAP) visualization of the ST data; spots are color coded based on cluster assignment.

(D) Dot plot showing the expression values of the main representative genes for each cluster identified.

RESULTS

Generation of the spatial gene expression dataset of skeletal muscle during ALS progression

Visium ST technology (10× Genomics) uses a grid of spots with uniquely barcoded oligo-dT primers to sample RNAs from an overlaid tissue section.[25,27] We applied this technology to spatially define gene expression in sections of tibialis anterior (TA) with the associated extensor digitorum longus (EDL) muscle of the SOD1^{G93A} mouse model of ALS (Figure 1A). Muscles were harvested at two different stages of the pathology, 75 and 150 days after birth, time points corresponding to the early and late stage of the disease. Wild-type (WT) littermates were used as a control. The number of Visium

CellPress
OPEN ACCESS

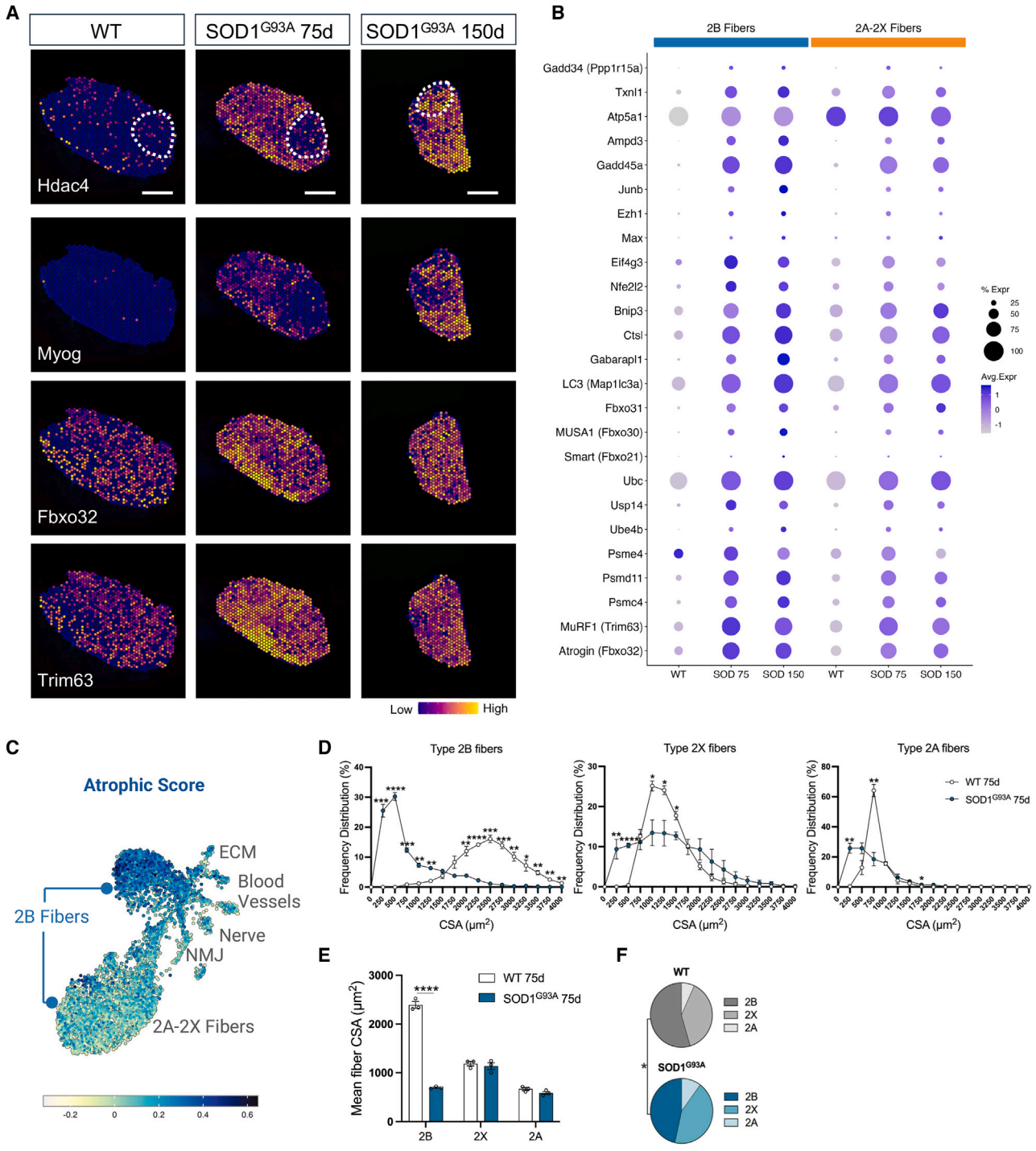

Figure 2. Vulnerability of glycolytic fibers during ALS progression

(A) Relative expression levels of Hdac4, Myog, Fbxo32, and Trim63 transcripts in muscles of WT and SOD1^{G93A} mice at 75 and 150 days of age. Scale bar, 1 mm (a dotted line highlights EDL muscle).

(B) Dot plot illustrating the relative expression and distribution of atrophy genes (atrogenes) in 2B (blue) and 2A-2X (orange) clusters in WT and SOD1^{G93A} mice at 75 and 150 days of age.

(C) UMAP visualization of the atrophic score in ST clusters.

(legend continued on next page)

spots varied among the muscle samples, ranging from 518 to 1,196 per section, and the mean number of genes detected per spot was 2,436. To visualize fiber boundaries, extracellular matrix scaffolds, and NMJs, we used anti-laminin and anti-collagen 1 antibodies and alpha-bungarotoxin (BTX), respectively (Figure 1B). As an internal control of the model, we evaluated SOD1, with 84% homology between human and murine transcripts, which is overexpressed in ALS-affected muscles (Figure 1B).

Graph-based clustering identified 10 main communities (Figure S1A), which were annotated based on expression of canonical markers, resulting in six major populations (Figures 1B, 1C, S1B, and S1C). For instance, the clusters shown in blue and orange correspond to the 2B and 2A-2X muscle fibers, respectively, while the clusters in violet, green, brown, and pink refer to the extracellular matrix (ECM), NMJ, nerves, and blood vessels, respectively (Figures 1B–1D, S1B, and S1C), largely mirroring the morphologically distinct regions identified in our previous study in mouse muscle samples.[26]

Thus, 2B fibers were identified by the expression of myosin heavy chain 4 (Myh4; fast glycolytic) and the fast isoform of tropomyosin (Tmp1). Of note, Amd1 and Smox, two enzymes responsible for polyamine biosynthesis, were detected in 2B fibers, in line with our previous study.[26] Myosin heavy chain 1 (Myh1; fast intermediate), myosin heavy chain 2 (Myh2; fast oxidative), lactate dehydrogenase b, and the myosin light chain 3, a marker of oxidative fibers, were the major contributors to the 2A-2X cluster. As expected, the collagen subunits (Col12a1, Col1a1) and ECM-associated molecules, such as fibromodulin and a matrix remodeler (Timp2), were used as markers to identify the ECM cluster. The NMJ cluster, on the other hand, was enriched for the acetylcholine receptor (AChR) subunits (Chrne, Chrnd, and Chrna1) and for genes known to be associated with the post-synaptic myofiber nuclei (Etv5), while the nerve domains were characterized by glial cell transcripts (Plp1, Pmp22, Mpz, and Mbp). Finally, endothelium- or smooth muscle-associated factors (CD31 [Pecam1], Tagln, Myh11, and Acta2) marked the vessel structures (Figure 1D). The number of spots in each cluster is indicated in Figure 1C. A comparison between ALS and WT muscles revealed changes in cluster abundance (Figures 1C, S1B, and S1C). A certain degree of heterogeneity was detected in both 2B fibers and 2A-2X fibers, which were composed of multiple clusters (Figures S1A and S1B). These clusters, while still expressing main canonical markers such as Myh4 or Myh2, displayed a marked condition-specific distribution. This most likely reflects the impact of the profound transcriptional changes occurring within the fiber during disease progression. The generated dataset is available for consultation at https://spatialmuscle.shinyapps.io/sam_app/.

Spatiotemporal regulation of atrophic signaling pathways in SOD1^{G93A} muscle fibers

Activation of the atrophic machinery in skeletal muscle is a critical event during the progression of ALS and indicates ongoing muscle denervation.[4] Indeed, we show that muscle fibers exhibit denervation and a decrease in their cross-sectional area (CSA) from the early stages of the disease (Figures S2A and S2B).

It has already been described that, depending on specific properties and metabolic pathways, muscles display a different vulnerability to atrophy; fast muscles are affected earlier, while slow muscles are more resistant.[21] In our dataset, we were able to detect the transcriptional activation of the atrophic program in different fibers within the same muscle. The expression of two of the main drivers of denervation-induced muscle atrophy, myogenin (Myog) and Hdac4,[34] was progressively activated in ALS muscle fibers (Figure 2A). Moreover, we detected the activation of Atrogin-1 (Fbxo32) and Murf1 (Trim63), two muscle-specific E3 ubiquitin ligases implicated in skeletal muscle atrophy (Figures 2A and S2C). Interestingly, with some exceptions, the transcriptional levels of atrogenes—transcripts commonly induced in atrophic conditions[35]—were higher in the 2B fiber cluster compared with the 2A-2X cluster (Figures 2A and 2B). This difference was already detectable at the early stage of the disease and, to a greater extent, toward the late stages, suggesting greater vulnerability of 2B fibers to atrophy in ALS muscles. Consistently, we observed increased atrophy, measured as an activation score relying on atrogene expression enrichment, in a subset of 2B fibers that progressively accumulates in ALS muscles (see Figures 2C and 1C as references).

In line with these data, as early as the onset of the pathology, we observed a pronounced reduction in CSA in the glycolytic type 2B fibers compared with the oxidative type 2A fibers and intermediate type 2X fibers, which remained essentially unchanged (Figures 2D, 2E, and S2D). By estimating the relative percentage of each fiber class, we detected a significant reduction in type 2B fibers in SOD1^{G93A} muscles (Figures 2F and S2D). Overall, these data identify glycolytic fibers as the most vulnerable type in ALS.

Fiber-type-specific alterations of the metabolic machinery in SOD1^{G93A} muscles

Given the differences in muscle fiber vulnerability within ALS muscles, we analyzed the most deregulated genes in the clusters corresponding to 2B and 2A-2X fibers. Consistent with our data reported above, 2B fibers activated denervation-induced genes (e.g., Myog, Gadd45a, and Runx1) (Figure S3A). Notably, a profound metabolic rearrangement was also observed. In line with a global increase in nicotinamide adenine dinucleotide-tetrazolium reductase (NADH-TR) positivity of SOD1^{G93A} TA sections (Figure S3B), we identified decreased Myh4 expression and increased Myh1 and Myh2 expression (Figures 3A

(D) Frequency distribution of type 2B, 2X, and 2A fibers CSA in TA muscle of WT and SOD1^{G93A} mice at 75 days of age. $n = 3$; values represent mean ± SEM; $^{*}p < 0.05$, $^{**}p < 0.01$, $^{***}p < 0.001$, $^{****}p < 0.0001$ by unpaired two-tailed t test.
(E) Mean CSA of type 2B, 2X, and 2A fibers in TA muscle of WT and SOD1^{G93A} mice at 75 days of age. $n = 3$, values represent mean ± SEM, $^{****}p < 0.0001$ by two-way ANOVA test.
(F) Pie charts illustrating the percentage of 2B-2X-2A fibers in TA muscle of WT and SOD1^{G93A} mice at 75 days of age. $n = 3$, $^{*}p < 0.05$ by unpaired two-tailed t test.

CellPress
OPEN ACCESS

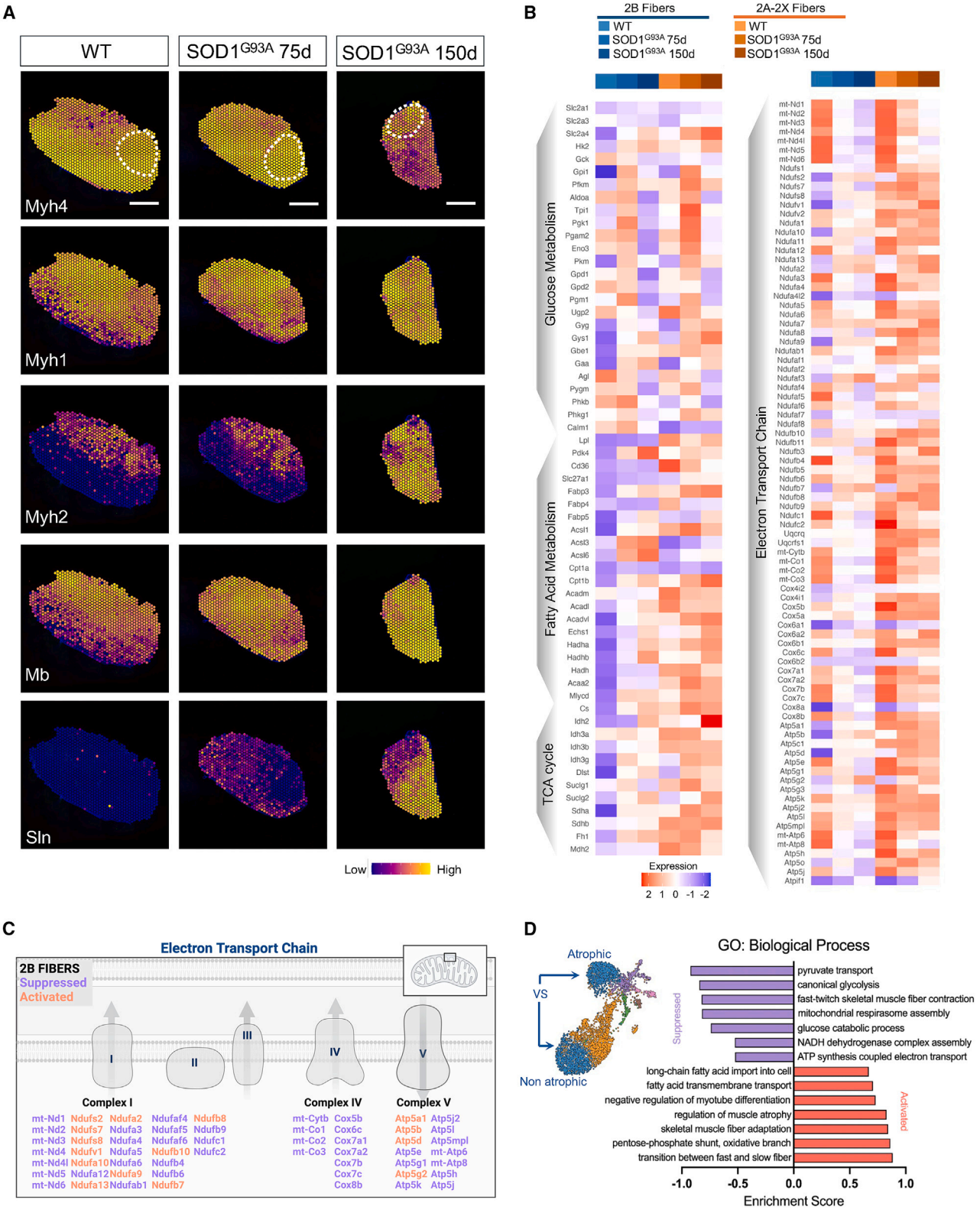

Figure 3. Metabolic reprogramming of muscle fibers in SOD1^{G93A} mice

(A) Relative expression levels of Myh4, Myh1, Myh2, Mb, and Sln transcripts in muscles of WT and SOD1^{G93A} mice at 75 and 150 days of age. Scale bar, 1 mm (a dotted line highlights EDL muscle).

(legend continued on next page)

and S3A). Additionally, elevated expression levels of myoglobin (Mb) and sarcolipin (Sln) suggested higher energy demand and a shift toward more oxidative metabolism (Figure 3A). While the expression of Mb was confined to the oxidative core of the TA under normal conditions, spatial analysis enabled us to detect its progressive spread to all of the muscle area during disease progression. Similarly, Sln expression, nearly absent in healthy muscle, increased dramatically throughout the SOD1^{G93A} fibers (Figure 3A).

Since the top deregulated genes in both clusters 2B and 2A-2X are essential for mitochondrial activity (e.g., mt-Atp8 and mt-Nd4l) (Figure S3A), we performed a detailed analysis of the changes in the energy production machinery in muscle fibers during ALS progression. To this end, we examined the main actors of glycolysis, fatty acid metabolism, the TCA cycle, and the electron transport chain (ETC) (Figures 3B and S3C). First, we observed an upregulation of genes regulating glucose metabolism at early stages of the disease in both 2B and 2A-2X clusters, while this transcriptional signature was absent during the late stages of the disease (Figure 3B). Furthermore, fatty acid metabolism and the TCA cycle, more active in the 2A-2X cluster than in 2B fibers of WT mice, showed progressive activation in 2B fibers of SOD1^{G93A} mice (Figure 3B), aligning with the increased energy demand associated with disease evolution. Interestingly, we observed a general repression of genes encoding for the ETC components, such as complex I, complex IV, and ATP synthase or complex V in the 2B fibers of SOD1^{G93A} mice (Figures 3B and 3C). Some of these changes were also evident in bulk RNA samples, confirming that metabolic changes could represent a potential early marker of ALS (Figure S3D). These results are consistent with the alterations in mitochondrial efficiency in ALS muscle reported previously by us and other groups.[10,16,36–38]

Gene ontology (GO) analysis revealed that the 2B fibers with a higher atrophic score displayed metabolic alterations. Beside the fast-to-slow transition, we also detected a repression of genes responsible for ATP synthesis (Figure 3D). Together, these findings highlight significant differences in the metabolic adaptations of 2B and 2A-2X muscle fibers during ALS, with a shift of 2B fibers toward oxidative metabolism and increased muscle energy requirements but with impaired mitochondrial functions. This underscores the profound metabolic reprogramming occurring in SOD1^{G93A} muscle fibers.

Polyamine pathway perturbations in ALS-related muscle dysfunction

As mentioned previously, Amd1, required for spermidine and spermine production, and Smox, necessary for spermine-to-spermidine conversion, are highly expressed in 2B fibers (Figure 1D). Given the increased vulnerability of 2B fibers in ALS and the dependence of polyamine homeostasis on innervation,[26] we speculated that the MN defect in ALS could result in an alteration of the polyamine synthesis machinery. To test this hypothesis, we analyzed the spatiotemporal expression of polyamine enzymes in TA muscles of SOD1^{G93A} mice at early and late stages of the disease. Indeed, disease progression was associated with a profound alteration in the expression of several polyamine enzymes throughout the muscle (Figures 4A and S4A). We observed the repression of Amd1 and Smox (Figures 4A and S4A), with Amd1 already found among the differentially expressed genes during disease progression (Figure S3A). The analysis of other components of the polyamine pathway, such as ornithine decarboxylase 1 (Odc1), the first rate-limiting enzyme in the synthesis of polyamines, and spermidine and spermine synthase (Srm and Sms, respectively) and Sat1, involved in the catabolic process of polyamines,[39,40] revealed their transcriptional induction to a greater extent in the 2B compared to the 2A-2X fiber compartment during disease progression (Figures 4A and S4A). Likewise, a strong upregulation of Oaz1 and Azin1, regulators of ODC1 activity,[41] occurred during the pathology (Figures 4A and S4A), confirming a global dysregulation of the pathway. Remarkably, one of the major components of the mammalian polyamine transport system, Atp13a3,[42,43] was found to be induced in ALS muscle compared with the WT (Figures 4A and S4A). We validated the expression levels of the aforementioned components of the polyamine pathway in whole muscles by PCR (Figures 4B–4D). Intriguingly, no notable changes in polyamine enzyme expression were detected in the spinal cord of SOD1^{G93A} mice at either stage of the disease (Figure S4B), suggesting that polyamine metabolism dysregulation is limited to the skeletal muscle compartment.

Polyamine homeostasis is tightly controlled by ODC1 and AMD1, which regulate their biogenesis. Given that ALS muscles are characterized by a concomitant induction of Odc1 and a reduction in Amd1/Amd2 expression, we speculated that these may reflect an imbalance in polyamine production. Indeed, as demonstrated by gas chromatography-mass spectrometry (GC-MS) quantitative analysis, we observed a drastic change in the ratio of polyamines in SOD1^{G93A} muscles (Figures 4C–4E). In TA, there was a significant increase in putrescine and spermidine, but not spermine, in both the pre-symptomatic and late stages of the disease (Figures 4C–4E, S4C, and S4D). The increased polyamine levels also correlate with the previously seen induction of Oaz1, known to be activated in response to high polyamine levels. It is interesting to note that alterations in Odc1, Amd1, Amd2, Smox, and Atp13a3 clearly correlate with atrophic 2B fibers appearing in SOD1^{G93A} muscle (Figure 4F). Finally, analysis of the overlapping deregulated genes in 2B fibers from SOD1^{G93A} and denervated muscle revealed a clear positive correlation between genes of the proteolytic machinery and polyamine metabolism (Figure S4E).

Slow muscles maintain a correct ratio of polyamines in ALS and denervation models

Next, we examined whether alterations in polyamine metabolism also affect slow muscles, known to be more resistant

(B) Heatmap illustrating the relative expression and distribution of metabolism-associated genes in 2B (blue) and 2A-2X (orange) clusters in WT and SOD1^{G93A} mice at 75 and 150 days of age.
(C) Diagram illustrating alterations in gene expression of the ETC in the 2B fibers of SOD1^{G93A} mice at 75 and 150 days of age.
(D) GO analysis of differentially expressed genes between atrophic and non-atrophic 2B fibers of WT and SOD1^{G93A} mice.

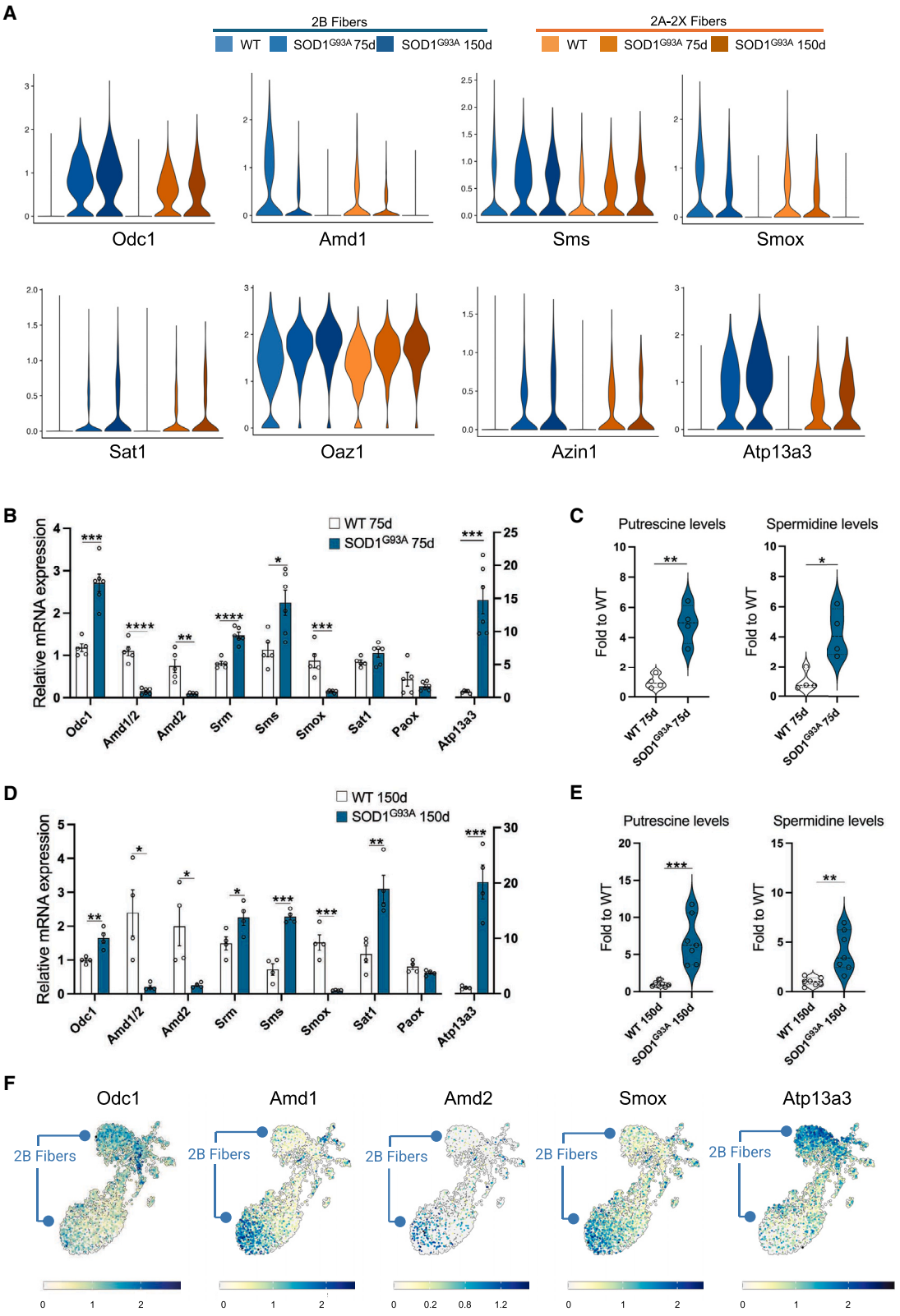

(legend on next page)

to the pathology and degenerate later during ALS progression. To this end, we analyzed the soleus, a purely oxidative muscle composed of a high percentage of type 1 slow fibers (Figures 5A and S5A). Notably, in SOD1^{G93A} mice at the early stage, the soleus remains innervated, with no change in muscle fiber CSA (Figures 5B–5D). At the stage of advanced disease, the soleus muscle is characterized by the presence of both atrophic and hypertrophic fibers (Figures S5A and S5B). Consistently, the induction of denervation-associated genes in the soleus was observed only during advanced disease, while in the TA muscle, it was evident at both 75 and 150 days of postnatal life (Figure S5C). Moreover, unlike the TA, the soleus does not present any alteration in polyamine enzyme gene expression at the early stage (Figure 5E) and only mild alteration at the late disease stage (Figure S5D). Accordingly, the GC-MS analysis did not reveal any differences in putrescine, spermidine, or spermine concentration in the soleus of SOD1^{G93A} mice in the early stage of disease compared to the WT (Figures 5F and S5E).

We described previously that, after acute (reversible) denervation, putrescine accumulates in TA muscles, while spermidine levels remain unchanged.[26] Conversely, in ALS, the chronic accumulation of putrescine in TA drives the accumulation of spermidine, overcoming the limitation of the substrate required for its formation due to Amd1/2 repression. To confirm this hypothesis, we took advantage of a model of prolonged (30 days) irreversible muscle denervation, based on resection of the sciatic nerve, that better resembles the ALS condition. Permanent denervation results in a strong reduction of the TA fiber CSA (Figures 5G and 5H) and a decrease of more than 50% of TA muscle mass compared to the control (CTR) (Figure 5I). This reduction was associated with altered expression of polyamine enzymes (Figure 5J) leading to putrescine, spermidine, and spermine accumulation in contrast to what was observed in the reversible denervation model (Figures 5K and S5F). Upon permanent resection of the sciatic nerve, the soleus, although completely denervated (Figure 5L), appeared to be less atrophic than the TA, as evaluated by measuring fiber size (40% vs. 58% of reduction in mean fiber CSA) and muscle mass 30 days after nerve damage (39.2% vs. 54.1% of reduction in muscle weight) (Figures 5M and 5N). Moreover, the soleus muscle displayed a more moderate induction of denervation-related genes (Sln, Myog, Hdac4, and Gadd45a) (Figure S5G) and less notable changes in the expression of polyamine enzymes, leading to a mild accumulation of putrescine with no significant accumulation of spermidine or spermine (Figures 5O, 5P, and S5H). These observations suggest that muscle resistance to atrophy and the regulation of polyamine metabolism are influenced not only by the loss of innervation but also by the specific fiber types within the muscle.

AMD1 inhibition triggers an ALS-like muscle phenotype

To assess whether alterations in the polyamine signaling pathway occur early, prior to the onset of symptomatic disease, we analyzed presymptomatic animals. In 45-day-old SOD1^{G93A} mice, TA muscle fibers were predominantly innervated (approximately 70%). Although the mean CSA of the fibers showed no significant reduction, certain fiber classes displayed a decrease in CSA. Remarkably, a significant reduction in Amd1, Amd2, and Smox expression was already detectable at this early disease stage (Figures S6A–S6C). Given that downregulation of the Amd1 transcript, which encodes for the S-adenosylmethionine decarboxylase (SAMDC), is an early event in the disease, we tested whether AMD1 (SAMDC) inhibition can lead to molecular changes in skeletal muscle fibers. We treated myotubes *in vitro* with sardomozide dihydrochloride,[44] an AMD1 inhibitor drug (experimental scheme shown in Figure 6A). Shown is a robust transcriptome change in myotubes treated with the AMD1 inhibitor, with 943 transcripts significantly induced and 1,063 reduced compared to CTR myotubes (Figures S6D–S6F). GO analysis of differentially expressed transcripts revealed RNA processing and oxidative phosphorylation as biological processes activated in treated myotubes, while muscle contraction and synapse maturation were identified as suppressed processes (Figure 6B). Primarily, it is noteworthy that inhibition of AMD1 also suppressed the polyamine pathway in treated cells, in line with the reduction in Smox expression (Figures 6B–6D). Furthermore, several genes implicated in NMJ formation were found to be dysregulated in the treated myotubes (Figures 6B and 6C). Specifically, downregulation of Etv5, Colq, Chrne, and Ache[45–47] was evident (Figure 6C). Additionally, we observed alterations in other genes known to be associated with neurological disorders (e.g., Cacna1h, Kcnc3, Scn3b, Atp1a3, and Atp1b2)[48–52] (Figure 6C) in treated myotubes. Simultaneously, genes involved in muscle contraction and sarcomere formation, including Tcap, Myoz1, Mybpc1, and Myot,[53,54] were repressed in AMD1 inhibitor-treated cells (Figure 6C). Moreover, transcripts related to mitochondrial dynamics (Nr4a3, Ppargc1a, and Mtfp1[55–57]) also showed altered expression in myotubes after AMD1 inhibitor treatment (Figure 6C). A dose-dependent effect of sardomozide was validated by qPCR for many of these genes (Figure 6D). The treatment was associated with a decrease in

Figure 4. Alteration in polyamine biosynthesis during ALS progression

(A) Violin plot showing the expression of Odc1, Amd1, Sms, Smox, Sat1, Oaz1, Azin1, and Atp13a3 transcripts in 2B (blue) and 2A-2X (orange) fiber clusters of WT, SOD1^{G93A} 75-day, and SOD1^{G93A} 150-day muscle.

(B) Relative expression of the Odc1, Amd1/2, Amd2, Srm, Sms, Smox, Sat1, Paox, and Atp13a3 genes in TA muscle of WT and SOD1^{G93A} mice at 75 days of age. $n = 5$ for WT, $n = 6$ for SOD1^{G93A}; values represent mean ± SEM; $^{*}p < 0.05$, $^{**}p < 0.01$, $^{***}p < 0.001$, $^{****}p < 0.0001$ by unpaired two-tailed t test.

(C) GC-MS quantitative analysis of putrescine and spermidine levels in WT and SOD1^{G93A} 75-day TA muscles. $n = 4$; $^{*}p < 0.05$, $^{**}p < 0.01$ by unpaired two-tailed t test.

(D) Relative expression of Odc1, Amd1/2, Amd2, Srm, Sms, Smox, Sat1, Paox, and Atp13a3 genes in TA muscle of WT and SOD1^{G93A} mice at 150 days of age. $n = 4$; values represent mean ± SEM; $^{*}p < 0.05$, $^{**}p < 0.01$, $^{***}p < 0.001$ by unpaired two-tailed t test.

(E) GC-MS quantitative analysis of putrescine and spermidine levels in WT and SOD1^{G93A} 150-day TA muscles. $n = 7$; $^{**}p < 0.01$, $^{***}p < 0.001$ by unpaired two-tailed t test.

(F) UMAP visualization of Odc1, Amd1, Amd2, Smox, and Atp13a3 transcript relative expression.

CellPress
OPEN ACCESS

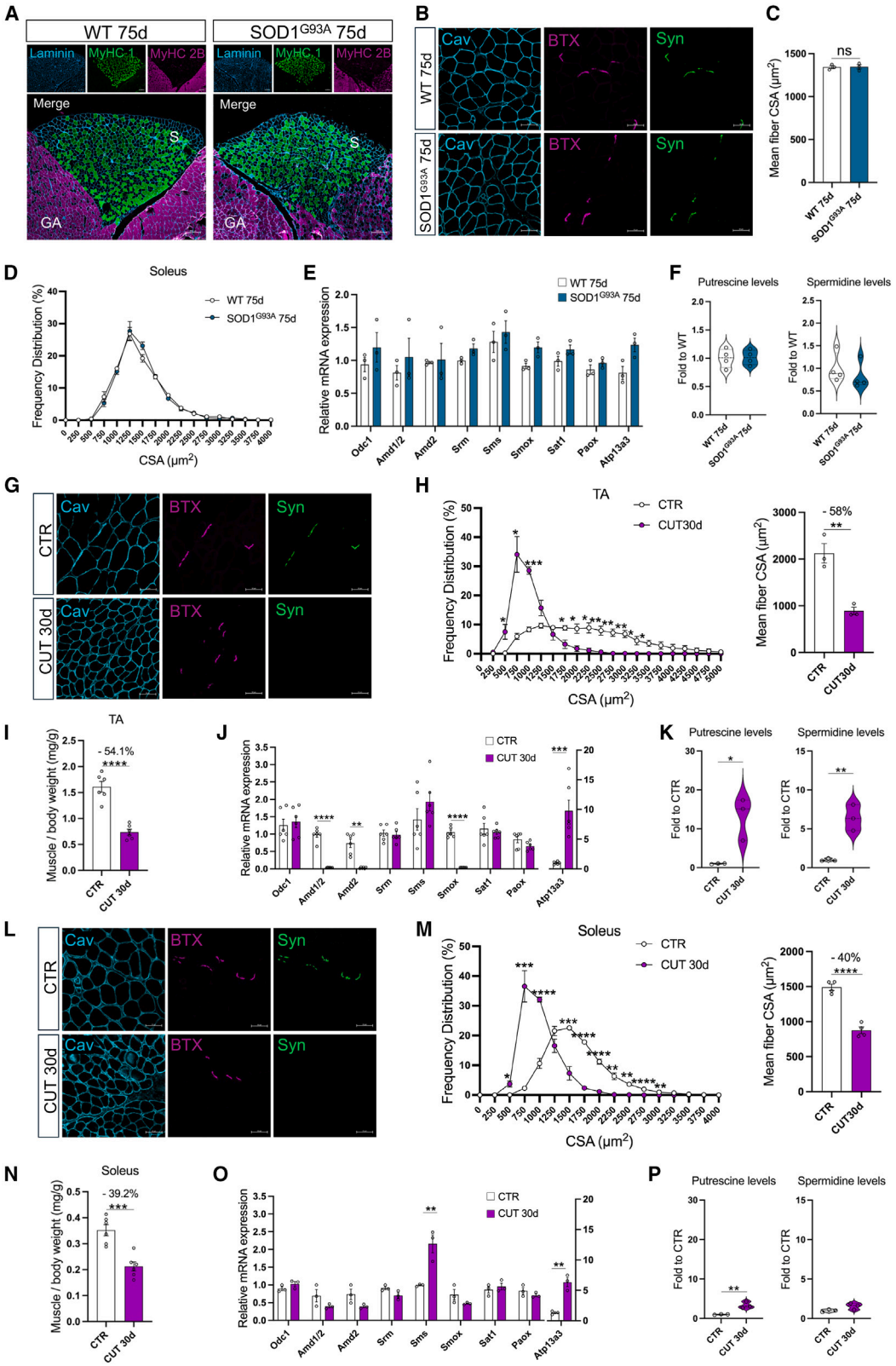

(legend on next page)

myotube diameter, evident 72 h after addition of the AMD1 inhibitor (Figure 6E).

Given the similarities between some features of the myotubes treated with the AMD1 inhibitor and ALS-affected skeletal muscle (e.g., the deregulation of Nr4a3, Ppargc1a, Ankrd1, and Mylk4 genes; Figures 6C, 6D, and S6G), we cross-referenced the transcriptional alterations of the sardomozide-treated myotubes with previously published transcriptome changes in the SOD1^{G93A} TA muscle. More than 130 genes show significant correlation in the two conditions (Figure S6H). GO analysis of transcripts showing similar alterations between sardomozide treatment and ALS revealed altered RNA processing and cell survival as well as suppression of biological processes associated with muscle function, protein stabilization, and, most interestingly, synapse organization (Figure 6F).

To explore whether AMD1 inhibition could trigger atrophy *in vivo*, WT mice were treated with the AMD1 inhibitor for 2 weeks via intraperitoneal injection (experimental scheme shown in Figure 6G). Although we observed no significant differences in body weight (Figure 6H), treated mice showed a decrease in TA muscle mass (Figure 6I) and a reduction in total muscle fiber CSA compared to CTR littermates (Figures 6J and 6K).

Overall, these findings suggest that disrupted polyamine metabolism due to AMD1 inhibition may contribute to muscle defects and atrophy observed in ALS.

Reduction of putrescine accumulation improves the muscle phenotype in SOD1^{G93A} mice

To investigate whether altered polyamine flux can be restored as a strategy to delay disease onset, we treated 50-day-old SOD1^{G93A} mice with the ODC1 inhibitor difluoromethylornithine (DFMO),[58] a US Food and Drug Administration (FDA)-approved drug for pediatric neuroblastoma, trypanosomiasis, and hirsutism[58–60] (the experimental plan is shown in Figure 7A). DFMO administration in drinking water halved the level of putrescine, but not spermidine or spermine, in skeletal muscle of SOD1^{G93A} mice (Figures 7B and S7A). No significant alteration in weight gain was observed during the 25 days of treatment (Figure S7B); however, the DFMO-treated mice displayed greater grip strength than CTRs (Figure 7C). Notably, while the CTR mice exhibited a decrease in strength of 20% or more, the DFMO-treated mice did not show loss of strength until the endpoint of the study (Figure 7D). Muscles were analyzed after treatment to assess muscle phenotype. As demonstrated, DFMO-treated mice presented increased weight of TA and gastrocnemius (GA) muscles compared to vehicle-treated mice (Figures 7E–7H). Additionally, DFMO-treated mice showed higher fiber CSA in both TA and GA muscles (Figures 7F, 7G, 7I, and 7J). Interestingly, the soleus muscle, in which polyamine levels remain unaltered, did not show significant changes in muscle mass and fiber CSA (Figures S7C and S7D). Moreover, in WT mice, the treatment had no effect on all parameters measured (Figures S7E–S7G), suggesting that ODC1 inhibition specifically impacts muscles with impaired polyamine metabolism and elevated Odc1 expression.

Taken together, these data demonstrate that targeting the polyamine flux in ALS could be a promising strategy, at least for preventing the muscle-associated disease phenotype.

DISCUSSION

Skeletal muscle and MNs form a functional unit through establishment of the NMJ. Both tissues cooperate to maintain homeostasis or in response to pathological conditions.[61,62] In this study, we revealed that altered muscle fiber innervation disrupts polyamine flux, impairing muscle homeostasis in ALS

Figure 5. Polyamine regulation in slow muscles

(A) Representative immunostaining for myosin heavy chain 1 (MyHC 1) (green), myosin heavy chain 2B (MyHC 2B) (violet), and laminin (cyan) of WT and SOD1^{G93A} 75-day GA and soleus (S) muscle sections. Scale bar, 200 μm.

(B) Representative immunostaining for caveolin-3 (Cav) (cyan) and synaptophysin (Syn) (green) of WT, SOD1^{G93A} 75-day soleus muscle sections; NMJs were stained with fluorescent BTX (violet). Scale bar, 50 μm.

(C) Mean CSA of fibers in soleus muscle of WT and SOD1^{G93A} mice at 75 days of age. $n = 3$; values represent mean ± SEM.

(D) Frequency distribution of fiber CSA in soleus muscle of WT and SOD1^{G93A} mice at 75 days of age. $n = 3$; values represent mean ± SEM.

(E) Relative expression of the Odc1, Amd1/2, Amd2, Srm, Sms, Smox, Sat1, Paox, and Atp13a3 genes in soleus muscle of WT and SOD1^{G93A} mice at 75 days of age. $n = 3$; values represent mean ± SEM.

(F) GC-MS quantitative analysis of putrescine and spermidine levels in WT and SOD1^{G93A} 75-day soleus muscles ($n = 4$).

(G) Representative immunostaining for Cav (cyan) and Syn (green) of control (CTR) and permanently denervated (CUT30d) TA muscle sections; NMJs were stained with fluorescent BTX (violet). Scale bar, 50 μm.

(H) Frequency distribution and mean CSA of fibers in TA muscle of CTR and CUT30d mice. $n = 3$; values represent mean ± SEM; $^{*}p < 0.05$, $^{**}p < 0.01$, $^{***}p < 0.001$ by unpaired two-tailed t test.

(I) Normalized TA muscle weight of CTR and CUT30d mice. $n = 6$; values represent mean ± SEM; $^{****}p < 0.0001$ by unpaired two-tailed t test.

(J) Relative expression of the Odc1, Amd1/2, Amd2, Srm, Sms, Smox, Sat1, Paox, and Atp13a3 genes in TA muscle of CTR and CUT30d mice. $n = 6$; values represent mean ± SEM; $^{**}p < 0.01$, $^{***}p < 0.001$, $^{****}p < 0.0001$ by unpaired two-tailed t test.

(K) GC-MS quantitative analysis of putrescine and spermidine levels in TA muscle of CTR and CUT30d mice. $n = 3$; $^{*}p < 0.05$, $^{**}p < 0.01$ by unpaired two-tailed t test.

(L) Representative immunostaining for Cav (cyan) and Syn (green) of CTR and CUT30d soleus muscle sections; NMJs were stained with fluorescent BTX (violet). Scale bar, 50 μm.

(M) Frequency distribution and mean CSA of fibers in soleus muscle of CTR and CUT30d mice. $n = 3$; values represent mean ± SEM; $^{*}p < 0.05$, $^{**}p < 0.01$, $^{***}p < 0.001$, $^{****}p < 0.0001$ by unpaired two-tailed t test.

(N) Normalized soleus muscle weight of CTR and CUT30d mice. $n = 6$; values represent mean ± SEM; $^{***}p < 0.001$ by unpaired two-tailed t test.

(O) Relative expression of Odc1, Amd1/2, Amd2, Srm, Sms, Smox, Sat1, Paox, and Atp13a3 genes in soleus muscle of CTR and CUT30d mice. $n = 3$; values represent mean ± SEM; $^{**}p < 0.01$ by unpaired two-tailed t test.

(P) GC-MS quantitative analysis of putrescine and spermidine levels in soleus muscle of CTR and CUT30d mice. $n = 3$, $^{**}p < 0.01$ by unpaired two-tailed t test.

CellPress
OPEN ACCESS

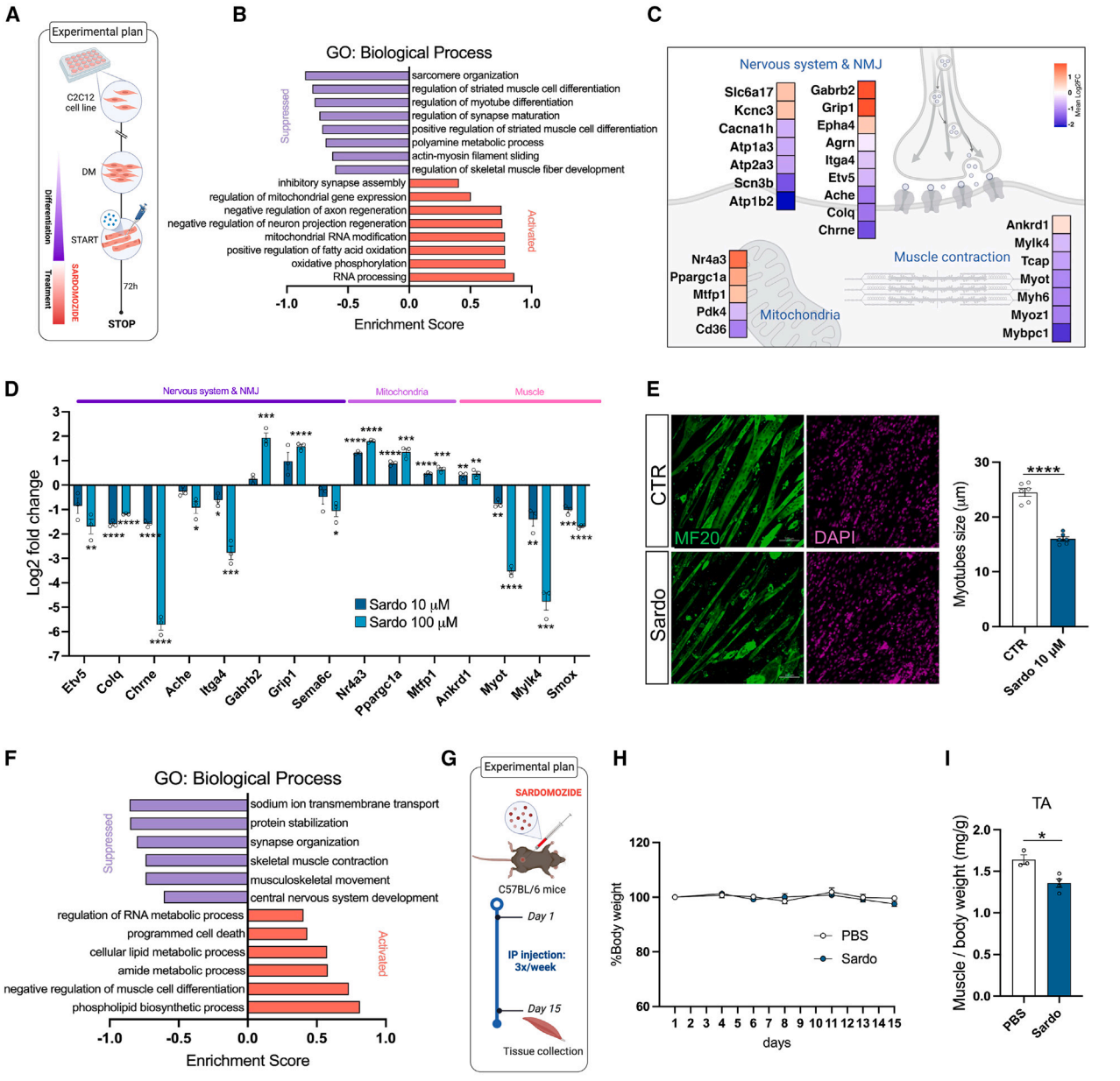

(legend on next page)

progression. Using the SOD1^{G93A} mouse model, we generated a spatial transcriptomic dataset of ALS skeletal muscle. Spatiotemporal analysis highlighted transcriptional changes within different muscle fiber types in the same muscle.

ALS pathology reveals differing vulnerabilities in MNs and muscles, with fast MNs and associated muscles degenerating earlier, while slow MNs and muscles show greater resistance. It remains unclear whether degeneration begins in MNs or muscle fibers. It has been demonstrated unequivocally that maintenance of NMJ stability through expression or stimulation of the postsynaptic Musk receptor can prolong MN survival by delaying denervation in mouse models of ALS.[15,63] In our study, we compared both different muscles and different fibers within the same muscle. We confirmed that, during ALS progression, the muscle phenotype is more severe in the fast muscle TA than in the slow muscle soleus. Both denervation and muscle atrophy are already present early, at 75 days after birth, in the TA, whereas the slow muscle appears to be less affected. Interestingly, using a permanent denervation mouse model, we show that, even after complete denervation, the soleus muscle is more resistant to muscle atrophy. In fact, while a 58% reduction was observed in the TA, a 40% reduction in CSA was found in the soleus. This difference, therefore, must necessarily be explained by disparity intrinsic to the muscle fibers and not by the MNs or the stability of the NMJ. In this case, analysis of what happens to fibers with different metabolism within the same muscle can give significant indication. As shown in TA muscle, there is a clear separation between an oxidative core consisting of type 2A and 2X fibers and a glycolytic cortex consisting of type 2B fibers. During ALS progression, while the oxidative core resists muscle atrophy, the type 2B fibers show reduced CSA and activation of catabolic signaling pathways. Indeed, ST revealed that atrogene activation is induced early in the glycolytic cluster and more intensely than in 2A-2X fibers. Along with atrophy induction, our results revealed significant metabolic reprogramming in SOD1^{G93A} muscle fibers. ALS is characterized by an increase in energy demand and general hypermetabolism.[64–68] Although neurons account for the increased energy demand, we show that glycolytic fibers shift toward an oxidative state characterized by the expression of Mb and Sln and the induction of lipid oxidation and the TCA cycle. This suggests an attempt to compensate for the muscle atrophy through increased fiber metabolic activity. Interestingly, in those fibers, a defect in ETC was observed, suggesting defective mitochondrial efficiency in ATP production. While it is speculative, these defects may explain the apparent paradox of why, although oxidative fibers are most protected from atrophy, glycolytic fibers that convert to an oxidative metabolism are the ones most affected by atrophy itself.

One of the major signaling pathways enriched in the glycolytic cortex is the polyamine synthesis machinery. Polyamines, small polycationic compounds with a positive charge, exist in three forms in mammalian cells: putrescine, spermidine, and spermine. Polyamine homeostasis is controlled meticulously by a series of enzymatic reactions. Fluctuations in polyamine concentrations and disturbances in their metabolism can inevitably have negative effects on overall health, potentially triggering and advancing pathological conditions such as neurological diseases or cancer.[39–42,69–72] We show that many of the genes responsible for controlling the polyamine flux are confined in 2B fibers of a healthy muscle. As demonstrated previously in acute denervation,[26] a severe alteration of the expression of genes regulating polyamine metabolism is also observed during ALS progression. An increase in the expression of Odc1, Srm, and Sms and a decrease in the expression of Amd1, Amd2, and Smox was observed. Strikingly, all of these alterations spatially correlate with altered energy metabolism and induction of atrophy. Moreover, an exceptional increase in the polyamine transporter Atp13a3 has been shown in the glycolytic fibers of SOD1^{G93A} muscle. These data, together with evidence showing that polyamine signaling is maintained in resistant soleus muscle, suggest that polyamine balance may participate in the establishment of the muscle phenotype in ALS. In agreement with this hypothesis, we observed that inhibition of AMD1, among the early enzymes downregulated in ALS muscle, results in the impairment of muscle function with the deregulation of transcripts associated with sarcomere formation and concomitant reduction of myotubes size. Intriguingly, downregulation of genes necessary for NMJ formation occurs upon AMD1 inhibition. This

Figure 6. Inhibition of AMD1 impairs muscle function

(A) Diagram of the experimental plan for sardomozide (Sardo) treatment on C2C12 myotubes.

(B) GO analysis of genes differentially expressed between vehicle (CTR) and Sardo-treated C2C12 myotubes.

(C) Representative diagram of genes differentially regulated between vehicle (CTR) and Sardo-treated C2C12 myotubes identified by RNA sequencing. Data are presented as a heatmap (log2-fold change). Red indicates higher expression; blue indicates lower expression.

(D) Relative expression of the indicated genes in Sardo-treated (10 and 100 μm) and vehicle (CTR)-treated C2C12 myotubes. $n = 3$; values represent mean ± SEM; $^{*}p < 0.05$, $^{**}p < 0.01$, $^{***}p < 0.001$, $^{****}p < 0.0001$ by unpaired two-tailed t test.

(E) Representative immunostaining for myosin (MF20, green) and DAPI (violet) of vehicle (CTR)-treated and Sardo-treated C2C12 myotubes. Scale bar, 100 μm. Quantification of myotubes diameter is shown in the graph (right). $n = 6$; values represent mean ± SEM; $^{****}p < 0.0001$ by unpaired two-tailed t test.

(F) GO analysis of differentially expressed genes with the same correlation between C2C12 myotubes treated with Sardo and SOD1^{G93A} TA muscle.

(G) Diagram of the experimental plan for Sardo treatment of WT mice.

(H) Graph showing the body weight (%) of vehicle-treated (PBS) and Sardo-treated WT mice ($n = 3$ for PBS, $n = 4$ for Sardo). Values represent mean ± SEM by two-way ANOVA test.

(I) Normalized TA muscle weight of vehicle-treated (PBS) and Sardo-treated WT mice ($n = 3$ for PBS, $n = 4$ for Sardo). Values represent mean ± SEM, $^{*}p < 0.05$ by unpaired two-tailed t test.

(J) Representative immunostaining for laminin (cyan) of TA sections of vehicle-treated (PBS) and Sardo-treated WT mice. Scale bar, 100 μm.

(K) Frequency distribution and mean CSA of fibers in TA muscle of vehicle-treated (PBS) and Sardo-treated WT mice ($n = 3$ for PBS, $n = 4$ for Sardo). Values represent mean ± SEM; $^{*}p < 0.05$, $^{**}p < 0.01$ by unpaired two-tailed t test.

CellPress
OPEN ACCESS

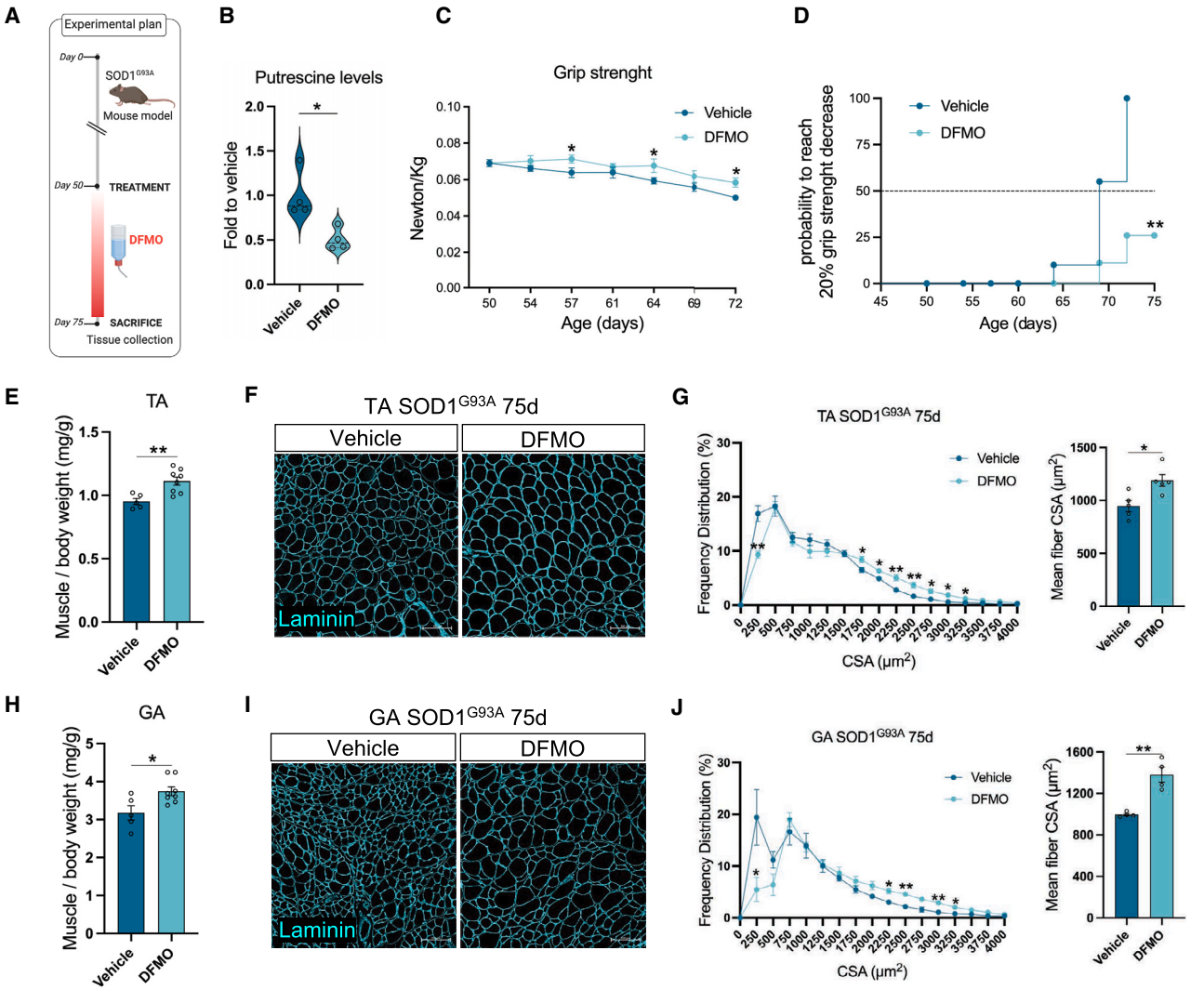

Figure 7. DFMO treatment prevents muscle phenotype progression in ALS mice

(A) Diagram of the experimental plan for difluoromethylornithine (DFMO) treatment of SOD1^{G93A} mice.

(B) GC-MS quantitative analysis of putrescine levels in TA muscle of vehicle- and DFMO-treated SOD1^{G93A} 75-day mice. $n = 4$, $^{*}p < 0.05$ by unpaired two-tailed t test.

(C) Dynamometric evaluation of grip strength in vehicle- and DFMO-treated SOD1^{G93A} mice. $n = 6$; values represent mean ± SEM; $^{*}p < 0.05$ by two-way ANOVA test.

(D) Kaplan-Meier curves representing when vehicle- and DFMO-treated SOD1^{G93A} mice had a muscular strength reduction of 20%. $n = 7$, $^{**}p < 0.01$ by log rank (Mantel-Cox) test.

(E) Normalized TA muscle weight of vehicle- and DFMO-treated SOD1^{G93A} 75-day mice ($n = 5$ for vehicle, $n = 8$ for DFMO). Values represent mean ± SEM; $^{**}p < 0.01$ by unpaired two-tailed t test.

(F) Representative immunostaining for laminin (cyan) of TA sections of vehicle- and DFMO-treated SOD1^{G93A} 75-day mice. Scale bar, 100 μm.

(G) Frequency distribution and mean CSA of fibers in TA muscle of vehicle- and DFMO-treated SOD1^{G93A} 75-day mice. $n = 5$; values represent mean ± SEM; $^{*}p < 0.05$, $^{**}p < 0.01$ by unpaired two-tailed t test.

(H) Normalized GA muscle weight of vehicle- and DFMO-treated SOD1^{G93A} 75-day mice ($n = 5$ for vehicle, $n = 8$ for DFMO). Values represent mean ± SEM; $^{*}p < 0.05$ by unpaired two-tailed t test.

(I) Representative immunostaining for laminin (cyan) of GA sections of vehicle- and DFMO-treated SOD1^{G93A} 75-day mice. Scale bar, 100 μm.

(J) Frequency distribution and mean CSA of fibers in GA muscle of vehicle- and DFMO-treated SOD1^{G93A} 75-day mice. $n = 4$; values represent mean ± SEM; $^{*}p < 0.05$, $^{**}p < 0.01$ by unpaired two-tailed t test.

observation reinforces the hypothesis that polyamine signaling pathway alteration could trigger some of the defects observed in ALS muscle. As proof of concept, we used an FDA-approved molecule to inhibit ODC1 activity and restore muscle homeostasis in ALS muscle. Although, in this work, we did not prove the efficacy of DFMO in lengthening the lifespan of SOD1^{G93A}

mice, we show promising results demonstrating that putrescine reduction caused by ODC1 inhibition prevents loss of muscle mass, promotes muscle strength, and increases fiber size. Ultimately, our work lays the foundation for the development of new therapeutic approaches in ALS based on the modulation of polyamine synthesis in skeletal muscle.

Limitations of the study

The study's reliance on a single genetic model, specifically the SOD1^{G93A} mutation, represents a notable limitation, as this mutation, though also identified in some sALS cases, may not fully capture the disease's broader genetic and phenotypic diversity. Additionally, the exclusive use of male mice limits the findings, particularly given established sex-related differences in ALS presentation and prevalence. Future research will address this by examining how sex influences polyamine regulation in ALS. Furthermore, we aim to extend DFMO treatment beyond disease onset to investigate its potential in not only enhancing initial muscle health but also in maintaining NMJ stability over time, which could support prolonged lifespan. Although previous studies suggest that enhanced muscle phenotype and delayed denervation may not increase life expectancy, systemic ODC1 inhibition might have broader implications by mitigating nervous system inflammation, offering promise for wider therapeutic applications. Last, ST resolution constraints are another limitation, but advancements in high-resolution ST could provide more detailed gene expression data at the single-cell level, illuminating the roles of underrepresented cell populations in ALS pathology.

RESOURCE AVAILABILITY

Lead contact

Requests for further information, resources, and reagents should be directed to and will be fulfilled by the lead contact, Luca Madaro (luca.madaro@uniroma1.it).

Materials availability

The reagents and materials for this study are available upon reasonable request.

Data and code availability

- All data reported in this paper will be shared by the lead contact upon request. Transcriptome raw data have been deposited in the GEO: GSE271011, GSE281403, and GSE271039. The ST dataset can be freely inspected on the Spatial ALS Muscle interactive platform (https://spatialmuscle.shinyapps.io/sam_app/).
- This paper re-analyzes existing, publicly available data. Accession numbers for these datasets are listed in the key resources table.
- All original code has been deposited on Zenodo: https://doi.org/10.5281/zenodo.14243515. All scripts to reproduce the analysis are submitted as supplemental information.

ACKNOWLEDGMENTS

This work was supported by AFM Research grants (#24349), PRIN 2022 (2022WN338R), and AIRC-MFAG (27578) (to L.M.); ANR (Agence Nationale de la Recherche) grants ANR-20-CE14-0048 and ANR-23-CE13-0030 (to L.G.); CNR IFT DBA.AD005.225-NUTRAGE- FOE2021, Italian Ministry of Health RF-2019-12369105, and PRIN 2022 Prot. 20223RXEEC (Italian Ministry of University and Research) (to A.F.) and PRIN 2022 Prot. 20222KSN2N (Italian Ministry of University and Research) (to C.V.).

AUTHOR CONTRIBUTIONS

Conceptualization, L.M. and L.G.; methodology, L.M., L.G., and V.R.; investigation, V.R., S.S., A.B., C.P., P.D., C.D., and C.C.; software, L.G. and A.B.; resources, S.S. and D.P.; writing – original draft, L.M., L.G., and V.R.; writing – review & editing, L.M., V.R., L.G., B.L.-O., L.L., A.F., C.V., A.M., and M.B.; funding acquisition, L.M., L.G., A.F., and C.V.

DECLARATION OF INTERESTS

L.G. carried out an ad hoc consultancy for EFFIK in 2024.

STAR★METHODS

Detailed methods are provided in the online version of this paper and include the following:

- KEY RESOURCES TABLE
- EXPERIMENTAL MODEL AND STUDY PARTICIPANT DETAILS
  - Mouse lines
  - DFMO treatment
  - Sardomozide treatment
- METHOD DETAILS
  - Denervation
  - Spatial Transcriptomics library preparation and analysis
  - RNA analysis by quantitative PCR
  - RNA-sequencing
  - Histological staining
  - C2C12 culture
  - Polyamine analysis
  - Figure design
- QUANTIFICATION AND STATISTICAL ANALYSIS
  - Statistical analysis

SUPPLEMENTAL INFORMATION

Supplemental information can be found online at https://doi.org/10.1016/j.celrep.2024.115123.

Received: July 4, 2024
Revised: November 11, 2024
Accepted: December 6, 2024

REFERENCES

1. Mead, R.J., Shan, N., Reiser, H.J., Marshall, F., and Shaw, P.J. (2023). Amyotrophic lateral sclerosis: a neurodegenerative disorder poised for successful therapeutic translation. Nat. Rev. Drug Discov. *22*, 185–212. https://doi.org/10.1038/s41573-022-00612-2.
2. Ryan, M., Heverin, M., McLaughlin, R.L., and Hardiman, O. (2019). Lifetime Risk and Heritability of Amyotrophic Lateral Sclerosis. JAMA Neurol. *76*, 1367–1374. https://doi.org/10.1001/JAMANEUROL.2019.2044.
3. Candelise, N., Salvatori, I., Scaricamazza, S., Nesci, V., Zenuni, H., Ferri, A., and Valle, C. (2022). Mechanistic Insights of Mitochondrial Dysfunction in Amyotrophic Lateral Sclerosis: An Update on a Lasting Relationship. Metabolites *12*, 233. https://doi.org/10.3390/METABO12030233.
4. Shefner, J.M., Musaro, A., Ngo, S.T., Lunetta, C., Steyn, F.J., Robitaille, R., De Carvalho, M., Rutkove, S., Ludolph, A.C., and Dupuis, L. (2023). Skeletal muscle in amyotrophic lateral sclerosis. Brain *146*, 4425–4436. https://doi.org/10.1093/BRAIN/AWAD202.
5. Killian, J.M., Wilfong, A.A., Burnett, L., Appel, S.H., and Boland, D. (1994). Decremental motor responses to repetitive nerve stimulation in ALS. Muscle Nerve *17*, 747–754. https://doi.org/10.1002/MUS.880170708.

6. De Carvalho, M., and Swash, M. (2013). Fasciculation potentials and earliest changes in motor unit physiology in ALS. J. Neurol. Neurosurg. Psychiatry *84*, 963–968. https://doi.org/10.1136/JNNP-2012-304545.

7. Fischer, L.R., Culver, D.G., Tennant, P., Davis, A.A., Wang, M., Castellano-Sanchez, A., Khan, J., Polak, M.A., and Glass, J.D. (2004). Amyotrophic lateral sclerosis is a distal axonopathy: Evidence in mice and man. Exp. Neurol. *185*, 232–240. https://doi.org/10.1016/J.EXPNEUROL.2003.10.004.

8. Moloney, E.B., de Winter, F., and Verhaagen, J. (2014). ALS as a distal axonopathy: molecular mechanisms affecting neuromuscular junction stability in the presymptomatic stages of the disease. Front. Neurosci. *8*, 252. https://doi.org/10.3389/FNINS.2014.00252.

9. Cappello, V., and Francolini, M. (2017). Neuromuscular Junction Dismantling in Amyotrophic Lateral Sclerosis. Int. J. Mol. Sci. *18*, 2092. https://doi.org/10.3390/IJMS18102092.

10. Scaricamazza, S., Salvatori, I., Giacovazzo, G., Loeffler, J.P., Renè, F., Rosina, M., Quessada, C., Proietti, D., Heil, C., Rossi, S., et al. (2020). Skeletal-Muscle Metabolic Reprogramming in ALS-SOD1G93A Mice Predates Disease Onset and Is A Promising Therapeutic Target. iScience *23*, 101087. https://doi.org/10.1016/J.ISCI.2020.101087.

11. Picchiarelli, G., Demestre, M., Zuko, A., Been, M., Higelin, J., Dieterlé, S., Goy, M.A., Mallik, M., Sellier, C., Scekic-Zahirovic, J., et al. (2019). FUS-mediated regulation of acetylcholine receptor transcription at neuromuscular junctions is compromised in amyotrophic lateral sclerosis. Nat. Neurosci. *22*, 1793–1805. https://doi.org/10.1038/S41593-019-0498-9.

12. Dobrowolny, G., Aucello, M., Rizzuto, E., Beccafico, S., Mammucari, C., Boncompagni, S., Belia, S., Wannenes, F., Nicoletti, C., Del Prete, Z., et al. (2008). Skeletal Muscle Is a Primary Target of SOD1G93A-Mediated Toxicity. Cell Metab. *8*, 425–436. https://doi.org/10.1016/J.CMET.2008.09.002.

13. Palamiuc, L., Schlagowski, A., Ngo, S.T., Vernay, A., Dirrig-Grosch, S., Henriques, A., Boutillier, A.L., Zoll, J., Echaniz-Laguna, A., Loeffler, J.P., and René, F. (2015). A metabolic switch toward lipid use in glycolytic muscle is an early pathologic event in a mouse model of amyotrophic lateral sclerosis. EMBO Mol. Med. *7*, 526–546. https://doi.org/10.15252/EMMM.201404433.

14. Zhou, B., Zheng, Y., Li, X., Dong, H., Yu, J., Zou, Y., Zhu, M., Yu, Y., Fang, X., Zhou, M., et al. (2022). FUS Mutation Causes Disordered Lipid Metabolism in Skeletal Muscle Associated with ALS. Mol. Neurobiol. *59*, 7265–7277. https://doi.org/10.1007/S12035-022-03048-2.

15. Pérez-García, M.J., and Burden, S.J. (2012). Increasing MuSK Activity Delays Denervation and Improves Motor Function in ALS Mice. Cell Rep. *2*, 497–502. https://doi.org/10.1016/J.CELREP.2012.08.004.

16. Genin, E.C., Madji Hounoum, B., Bannwarth, S., Fragaki, K., Lacas-Gervais, S., Mauri-Crouzet, A., Lespinasse, F., Neveu, J., Ropert, B., Augé, G., et al. (2019). Mitochondrial defect in muscle precedes neuromuscular junction degeneration and motor neuron death in CHCHD10 S59L/+ mouse. Acta Neuropathol. *138*, 123–145. https://doi.org/10.1007/S00401-019-01988-Z.

17. Wong, M., and Martin, L.J. (2010). Skeletal muscle-restricted expression of human SOD1 causes motor neuron degeneration in transgenic mice. Hum. Mol. Genet. *19*, 2284–2302. https://doi.org/10.1093/HMG/DDQ106.

18. Frey, D., Schneider, C., Xu, L., Borg, J., Spooren, W., and Caroni, P. (2000). Early and selective loss of neuromuscular synapse subtypes with low sprouting competence in motoneuron diseases. J. Neurosci. *20*, 2534–2542. https://doi.org/10.1523/JNEUROSCI.20-07-02534.2000.

19. Talbot, J., and Maves, L. (2016). Skeletal muscle fiber type: using insights from muscle developmental biology to dissect targets for susceptibility and resistance to muscle disease. Wiley Interdiscip. Rev. Dev. Biol. *5*, 518–534. https://doi.org/10.1002/WDEV.230.

20. Schweingruber, C., and Hedlund, E. (2022). The Cell Autonomous and Non-Cell Autonomous Aspects of Neuronal Vulnerability and Resilience in Amyotrophic Lateral Sclerosis. Biology *11*, 1191. https://doi.org/10.3390/BIOLOGY11081191.

21. Nijssen, J., Comley, L.H., and Hedlund, E. (2017). Motor neuron vulnerability and resistance in amyotrophic lateral sclerosis. Acta Neuropathol. *133*, 863–885. https://doi.org/10.1007/S00401-017-1708-8.

22. Hegedus, J., Putman, C.T., and Gordon, T. (2007). Time course of preferential motor unit loss in the SOD1 G93A mouse model of amyotrophic lateral sclerosis. Neurobiol. Dis. *28*, 154–164. https://doi.org/10.1016/J.NBD.2007.07.003.

23. Hegedus, J., Putman, C.T., Tyreman, N., and Gordon, T. (2008). Preferential motor unit loss in the SOD1 G93A transgenic mouse model of amyotrophic lateral sclerosis. J. Physiol. *586*, 3337–3351. https://doi.org/10.1113/JPHYSIOL.2007.149286.

24. Hedlund, E., Karlsson, M., Osborn, T., Ludwig, W., and Isacson, O. (2010). Global gene expression profiling of somatic motor neuron populations with different vulnerability identify molecules and pathways of degeneration and protection. Brain *133*, 2313–2330. https://doi.org/10.1093/BRAIN/AWQ167.

25. Du, J., Yang, Y.C., An, Z.J., Zhang, M.H., Fu, X.H., Huang, Z.F., Yuan, Y., and Hou, J. (2023). Advances in spatial transcriptomics and related data analysis strategies. J. Transl. Med. *21*, 330. https://doi.org/10.1186/S12967-023-04150-2.

26. D'Ercole, C., D'Angelo, P., Ruggieri, V., Proietti, D., Virtanen, L., Parisi, C., Riera, C.S., Renzini, A., Macone, A., Marzullo, M., et al. (2022). Spatially resolved transcriptomics reveals innervation-responsive functional clusters in skeletal muscle. Cell Rep. *41*, 111861. https://doi.org/10.1016/J.CELREP.2022.111861.

27. Ståhl, P.L., Salmén, F., Vickovic, S., Lundmark, A., Navarro, J.F., Magnusson, J., Giacomello, S., Asp, M., Westholm, J.O., Huss, M., et al. (2016). Visualization and analysis of gene expression in tissue sections by spatial transcriptomics. Science *353*, 78–82. https://doi.org/10.1126/SCIENCE.AAF2403.

28. Hsu, J.-E., Ruiz, L., Hwang, Y., Guzman, S., Cho, C.-S., Cheng, W., Si, Y., Macpherson, P., Schrank, M., Jun, G., et al. (2024). High-Resolution Spatial Transcriptomic Atlas of Mouse Soleus Muscle: Unveiling Single Cell and Subcellular Heterogeneity in Health and Denervation. bioRxiv *2024*, 2024.02.26.582103. https://doi.org/10.1101/2024.02.26.582103.

29. Stec, M.J., Su, Q., Adler, C., Zhang, L., Golann, D.R., Khan, N.P., Panagis, L., Villalta, S.A., Ni, M., Wei, Y., et al. (2023). A cellular and molecular spatial atlas of dystrophic muscle. Proc. Natl. Acad. Sci. USA *120*, e2221249120. https://doi.org/10.1073/PNAS.2221249120.

30. Lequain, H., Dégletagne, C., Streichenberger, N., Valantin, J., Simonet, T., Schaeffer, L., Sève, P., and Leblanc, P. (2023). Spatial Transcriptomics Reveals Signatures of Histopathological Changes in Muscular Sarcoidosis. Cells *12*, 2747. https://doi.org/10.3390/CELLS12232747.

31. Heezen, L.G.M., Abdelaal, T., van Putten, M., Aartsma-Rus, A., Mahfouz, A., and Spitali, P. (2023). Spatial transcriptomics reveal markers of histopathological changes in Duchenne muscular dystrophy mouse models. Nat. Commun. *14*, 4909. https://doi.org/10.1038/S41467-023-40555-9.

32. Coulis, G., Jaime, D., Guerrero-Juarez, C., Kastenschmidt, J.M., Farahat, P.K., Nguyen, Q., Pervolarakis, N., McLinden, K., Thurlow, L., Movahedi, S., et al. (2023). Single-cell and spatial transcriptomics identify a macrophage population associated with skeletal muscle fibrosis. Sci. Adv. *9*, eadd9984. https://doi.org/10.1126/SCIADV.ADD9984.

33. Wang, Z., Khondowe, P., Brannick, E., and Abasht, B. (2024). Spatial transcriptomics reveals alterations in perivascular macrophage lipid metabolism in the onset of Wooden Breast myopathy in broiler chickens. Sci. Rep. *14*, 3450. https://doi.org/10.1038/S41598-024-53904-5.

34. Moresi, V., Williams, A.H., Meadows, E., Flynn, J.M., Potthoff, M.J., McAnally, J., Shelton, J.M., Backs, J., Klein, W.H., Richardson, J.A., et al. (2010). Myogenin and class II HDACs control neurogenic muscle atrophy by inducing E3 ubiquitin ligases. Cell *143*, 35–45. https://doi.org/10.1016/J.CELL.2010.09.004.

35. Lecker, S.H., Jagoe, R.T., Gilbert, A., Gomes, M., Baracos, V., Bailey, J., Price, S.R., Mitch, W.E., and Goldberg, A.L. (2004). Multiple types of skeletal muscle atrophy involve a common program of changes in

gene expression. FASEB J. *18*, 39–51. https://doi.org/10.1096/FJ.03-0610COM.

36. Xiao, Y., Karam, C., Yi, J., Zhang, L., Li, X., Yoon, D., Wang, H., Dhakal, K., Ramlow, P., Yu, T., et al. (2018). ROS-related mitochondrial dysfunction in skeletal muscle of an ALS mouse model during the disease progression. Pharmacol. Res. *138*, 25–36. https://doi.org/10.1016/J.PHRS.2018.09.008.
37. Wiedemann, F.R., Winkler, K., Kuznetsov, A.V., Bartels, C., Vielhaber, S., Feistner, H., and Kunz, W.S. (1998). Impairment of mitochondrial function in skeletal muscle of patients with amyotrophic lateral sclerosis. J. Neurol. Sci. *156*, 65–72. https://doi.org/10.1016/S0022-510X(98)00008-2.
38. Luo, G., Yi, J., Ma, C., Xiao, Y., Yi, F., Yu, T., and Zhou, J. (2013). Defective Mitochondrial Dynamics Is an Early Event in Skeletal Muscle of an Amyotrophic Lateral Sclerosis Mouse Model. PLoS One *8*, e82112. https://doi.org/10.1371/JOURNAL.PONE.0082112.
39. Holbert, C.E., Cullen, M.T., Casero, R.A., and Stewart, T.M. (2022). Polyamines in cancer: integrating organismal metabolism and antitumour immunity. Nat. Rev. Cancer *22*, 467–480. https://doi.org/10.1038/s41568-022-00473-2.
40. Xuan, M., Gu, X., Li, J., Huang, D., Xue, C., and He, Y. (2023). Polyamines: their significance for maintaining health and contributing to diseases. Cell Commun. Signal. *21*, 348. https://doi.org/10.1186/S12964-023-01373-0.
41. Casero, R.A., Murray Stewart, T., and Pegg, A.E. (2018). Polyamine metabolism and cancer: treatments, challenges and opportunities. Nat. Rev. Cancer *18*, 681–695. https://doi.org/10.1038/S41568-018-0050-3.
42. Sekhar, V., Andl, T., and Phanstiel, O. (2022). ATP13A3 facilitates polyamine transport in human pancreatic cancer cells. Sci. Rep. *12*, 4045. https://doi.org/10.1038/s41598-022-07712-4.
43. Hamouda, N.N., van den Haute, C., Vanhoutte, R., Sannerud, R., Azfar, M., Mayer, R., Cortés Calabuig, Á., Swinnen, J.V., Agostinis, P., Baekelandt, V., et al. (2021). ATP13A3 is a major component of the enigmatic mammalian polyamine transport system. J. Biol. Chem. *296*, 100182. https://doi.org/10.1074/JBC.RA120.013908.
44. Regenass, U., Mett, H., Stanek, J., Mueller, M., Kramer, D., and Porter, C.W. (1994). CGP 48664, a new S-adenosylmethionine decarboxylase inhibitor with broad spectrum antiproliferative and antitumor activity. Cancer Res. *54*, 3210. https://pubmed.ncbi.nlm.nih.gov/8205541/.
45. Petrany, M.J., Swoboda, C.O., Sun, C., Chetal, K., Chen, X., Weirauch, M.T., Salomonis, N., and Millay, D.P. (2020). Single-nucleus RNA-seq identifies transcriptional heterogeneity in multinucleated skeletal myofibers. Nat. Commun. *11*, 6374. https://doi.org/10.1038/s41467-020-20063-w.
46. Kim, M., Franke, V., Brandt, B., Lowenstein, E.D., Schöwel, V., Spuler, S., Akalin, A., and Birchmeier, C. (2020). Single-nucleus transcriptomics reveals functional compartmentalization in syncytial skeletal muscle cells. Nat. Commun. *11*, 6375. https://doi.org/10.1038/S41467-020-20064-9.
47. Ham, A.S., Lin, S., Tse, A., Thürkauf, M., Oliveri, F., and Rüegg, M.A. (2024). Single-nuclei sequencing of skeletal muscle reveals subsynaptic-specific transcripts involved in neuromuscular junction maintenance. bioRxiv. https://doi.org/10.1101/2024.05.15.594276.
48. Delers, P., Sapaly, D., Salman, B., De Waard, S., De Waard, M., and Lefebvre, S. (2022). A link between agrin signalling and Cav3.2 at the neuromuscular junction in spinal muscular atrophy. Sci. Rep. *12*, 18960. https://doi.org/10.1038/S41598-022-23703-X.
49. Waters, M.F., Minassian, N.A., Stevanin, G., Figueroa, K.P., Bannister, J.P.A., Nolte, D., Mock, A.F., Evidente, V.G.H., Fee, D.B., Müller, U., et al. (2006). Mutations in voltage-gated potassium channel KCNC3 cause degenerative and developmental central nervous system phenotypes. Nat. Genet. *38*, 447–451. https://doi.org/10.1038/NG1758.
50. Nutini, M., Spalloni, A., Florenzano, F., Westenbroek, R.E., Marini, C., Catterall, W.A., Bernardi, G., and Longone, P. (2011). Increased expression of the beta3 subunit of voltage-gated Na+ channels in the spinal cord of the SOD1G93A mouse. Mol. Cell. Neurosci. *47*, 108–118. https://doi.org/10.1016/J.MCN.2011.03.005.
51. Sweadner, K.J., Toro, C., Whitlow, C.T., Snively, B.M., Cook, J.F., Ozelius, L.J., Markello, T.C., and Brashear, A. (2016). ATP1A3 Mutation in Adult Rapid-Onset Ataxia. PLoS One *11*, e0151429. https://doi.org/10.1371/JOURNAL.PONE.0151429.
52. Salemi, M., Ravo, M., Lanza, G., Schillaci, F.A., Ventola, G.M., Marchese, G., Salluzzo, M.G., Cappelletti, G., and Ferri, R. (2024). Gene Expression Profiling of Post Mortem Midbrain of Parkinson's Disease Patients and Healthy Controls. Int. J. Mol. Sci. *25*, 707. https://doi.org/10.3390/IJMS25020707.
53. Gautel, M., and Djinović-Carugo, K. (2016). The sarcomeric cytoskeleton: from molecules to motion. J. Experim. Biol. *219*, 135–145. https://doi.org/10.1242/JEB.124941.
54. Hessel, A.L., Engels, N.M., Kuehn, M.N., Nissen, D., Sadler, R.L., Ma, W., Irving, T.C., Linke, W.A., and Harris, S.P. (2024). Myosin-binding protein C regulates the sarcomere lattice and stabilizes the OFF states of myosin heads. Nat. Commun. *15*, 2628. https://doi.org/10.1038/s41467-024-46957-7.
55. Qian, L., Zhu, Y., Deng, C., Liang, Z., Chen, J., Chen, Y., Wang, X., Liu, Y., Tian, Y., and Yang, Y. (2024). Peroxisome proliferator-activated receptor gamma coactivator-1 (PGC-1) family in physiological and pathophysiological process and diseases. Signal Transduct. Target. Ther. *9*, 50. https://doi.org/10.1038/s41392-024-01756-w.
56. Donnarumma, E., Kohlhaas, M., Vimont, E., Kornobis, E., Chaze, T., Gianetto, Q.G., Matondo, M., Moya-Nilges, M., Maack, C., and Wai, T. (2022). Mitochondrial Fission Process 1 controls inner membrane integrity and protects against heart failure. Nat. Commun. *13*, 6634. https://doi.org/10.1038/s41467-022-34316-3.
57. Paez, H.G., Pitzer, C.R., Ferrandi, P.J., Mohamed, J.S., and Alway, S.E. (2022). NOR-1 Knockdown Reduces Mitochondrial Function in C2C12 Myotubes. FASEB J. *36*, 1. https://doi.org/10.1096/FASEBJ.2022.36.S1.R2545.
58. Sholler, G.L.S., Ferguson, W., Bergendahl, G., Bond, J.P., Neville, K., Eslin, D., Brown, V., Roberts, W., Wada, R.K., Oesterheld, J., et al. (2018). Maintenance DFMO Increases Survival in High Risk Neuroblastoma. Sci. Rep. *8*, 14445. https://doi.org/10.1038/s41598-018-32659-w.
59. Jackson, J., Caro, J.J., Caro, G., Garfield, F., Huber, F., Zhou, W., Lin, C.S., Shander, D., and Schrode, K.; Eflornithine HCl Study Group (2007). The effect of eflornithine 13.9% cream on the bother and discomfort due to hirsutism. Int. J. Dermatol. *46*, 976–981. https://doi.org/10.1111/J.1365-4632.2007.03270.X.
60. Priotto, G., Pinoges, L., Fursa, I.B., Burke, B., Nicolay, N., Grillet, G., Hewison, C., and Balasegaram, M. (2008). Safety and effectiveness of first line eflornithine for Trypanosoma brucei gambiense sleeping sickness in Sudan: cohort study. BMJ *336*, 705–708. https://doi.org/10.1136/BMJ.39485.592674.BE.
61. Li, L., Xiong, W.C., and Mei, L. (2018). Neuromuscular Junction Formation, Aging, and Disorders. Annu. Rev. Physiol. *80*, 159–188. https://doi.org/10.1146/ANNUREV-PHYSIOL-022516-034255.
62. Sanes, J.R., and Lichtman, J.W. (2001). Induction, assembly, maturation and maintenance of a postsynaptic apparatus. Nat. Rev. Neurosci. *2*, 791–805. https://doi.org/10.1038/35097557.
63. Cantor, S., Zhang, W., Delestrée, N., Remédio, L., Mentis, G.Z., and Burden, S.J. (2018). Preserving neuromuscular synapses in ALS by stimulating MuSK with a therapeutic agonist antibody. Elife *7*, e34375. https://doi.org/10.7554/ELIFE.34375.
64. Desport, J.C., Torny, F., Lacoste, M., Preux, P.M., and Couratier, P. (2005). Hypermetabolism in ALS: Correlations with clinical and paraclinical parameters. Neurodegener. Dis. *2*, 202–207. https://doi.org/10.1159/000089626.
65. Steyn, F.J., Ioannides, Z.A., Van Eijk, R.P.A., Heggie, S., Thorpe, K.A., Ceslis, A., Heshmat, S., Henders, A.K., Wray, N.R., Van Den Berg, L.H., et al.

(2018). Research paper: Hypermetabolism in ALS is associated with greater functional decline and shorter survival. J. Neurol. Neurosurg. Psychiatry *89*, 1016–1023. https://doi.org/10.1136/JNNP-2017-317887.

66. Bouteloup, C., Desport, J.C., Clavelou, P., Guy, N., Derumeaux-Burel, H., Ferrier, A., and Couratier, P. (2009). Hypermetabolism in ALS patients: An early and persistent phenomenon. J. Neurol. *256*, 1236–1242. https://doi.org/10.1007/S00415-009-5100-Z.
67. Dupuis, L., Pradat, P.F., Ludolph, A.C., and Loeffler, J.P. (2011). Energy metabolism in amyotrophic lateral sclerosis. Lancet Neurol. *10*, 75–82. https://doi.org/10.1016/S1474-4422(10)70224-6.
68. Desport, J.C., Preux, P.M., Magy, L., Boirie, Y., Vallat, J.M., Beaufrère, B., and Couratier, P. (2001). Factors correlated with hypermetabolism in patients with amyotrophic lateral sclerosis. Am. J. Clin. Nutr. *74*, 328–334. https://doi.org/10.1093/AJCN/74.3.328.
69. Rodan, L.H., Anyane-Yeboa, K., Chong, K., Klein Wassink-Ruiter, J.S., Wilson, A., Smith, L., Kothare, S.V., Rajabi, F., Blaser, S., Ni, M., et al. (2018). Gain-of-function variants in the ODC1 gene cause a syndromic neurodevelopmental disorder associated with macrocephaly, alopecia, dysmorphic features, and neuroimaging abnormalities. Am. J. Med. Genet. *176*, 2554–2560. https://doi.org/10.1002/AJMG.A.60677.
70. Tao, X., Liu, J., Diaz-Perez, Z., Foley, J.R., Nwafor, A., Stewart, T.M., Casero, R.A., and Zhai, R.G. (2024). Reduction of spermine synthase enhances autophagy to suppress Tau accumulation. Cell Death Dis. *15*, 333. https://doi.org/10.1038/S41419-024-06720-8.
71. Li, C., Brazill, J.M., Liu, S., Bello, C., Zhu, Y., Morimoto, M., Cascio, L., Pauly, R., Diaz-Perez, Z., Malicdan, M.C.V., et al. (2017). Spermine synthase deficiency causes lysosomal dysfunction and oxidative stress in models of Snyder-Robinson syndrome. Nat. Commun. *8*, 1257. https://doi.org/10.1038/S41467-017-01289-7.
72. Wolters-Eisfeld, G., Hackert, T., and Güngör, C. (2023). Unmasking metabolic dependencies in pancreatic cancer: aberrant polyamine synthesis as a promising new therapeutic target. Sig. Transduc. Target. Therapy *8*, 1–2. https://doi.org/10.1038/s41392-023-01662-7.
73. Schneider, C.A., Rasband, W.S., and Eliceiri, K.W. (2012). NIH Image to ImageJ: 25 years of image analysis. Nat. Methods *9*, 671–675. https://doi.org/10.1038/nmeth.2089.
74. Hao, Y., Hao, S., Andersen-Nissen, E., Mauck, W.M., Zheng, S., Butler, A., Lee, M.J., Wilk, A.J., Darby, C., Zager, M., et al. (2021). Integrated analysis of multimodal single-cell data. Cell *184*, 3573–3587.e29. https://doi.org/10.1016/J.CELL.2021.04.048.
75. Wickham, H., François, R., Henry, L., and Müller, K. (2022). Dplyr: A Grammar of Data Manipulation. https://dplyr.tidyverse.org.
76. Wilke, C., Fox, S.J., Bates, T., Manalo, K., Lang, B., Barrett, M., Stoiber, M., Philipp, A., Denney, B., Hesselberth, J., et al. (2021). Wilkelab/CowPlot: 1.1.1 (1.1.1), Zenodo. https://doi.org/10.5281/zenodo.4411966.
77. Wickham, H. (2016). Data Analysis, pp. 189–201. https://doi.org/10.1007/978-3-319-24277-4_9.
78. Slowikowski, K. (2024). ggrepel: Automatically Position Non-Overlapping Text Labels with 'ggplot2'. https://ggrepel.slowkow.com/.
79. Hafemeister, C., and Satija, R. (2019). Normalization and variance stabilization of single-cell RNA-seq data using regularized negative binomial regression. Genome Biol. *20*, 296. https://doi.org/10.1186/S13059-019-1874-1.
80. Pedersen, T. (2022). Patchwork: The Composer of Plots. https://patchwork.data-imaginist.com.
81. Garnier, S., Ross, N., Budis, B., Filipovic-Pierucci, A., Galili, T., Greenwell, B., Sievert, C., Harris, D.J., Sciaini, M., and Chen, J.J. (2021). Sjmgarnier/Viridis: CRAN release v0.6.2 (v0.6.2CRAN), Zenodo. https://doi.org/10.5281/zenodo.5579397.
82. Kolberg, L., Raudvere, U., Kuzmin, I., Vilo, J., and Peterson, H. (2020). gprofiler2 – an R package for gene list functional enrichment analysis and namespace conversion toolset g: Profiler. F1000Res. *9*, 709. https://doi.org/10.12688/F1000RESEARCH.24956.2/.
83. Wu, T., Hu, E., Xu, S., Chen, M., Guo, P., Dai, Z., Feng, T., Zhou, L., Tang, W., Zhan, L., et al. (2021). clusterProfiler 4.0: A universal enrichment tool for interpreting omics data. Innovation *2*, 100141. https://doi.org/10.1016/J.XINN.2021.100141.
84. Carlson, M. (2023). Org.Mm.eg.db 3.18.0. https://doi.org/10.18129/B9.bioc.org.Mm.eg.db.
85. Larsson, J. (2024). eulerr: Area-Proportional Euler and Venn Diagrams with Ellipses. R package version 7.0.2. https://CRAN.R-project.org/package=eulerr.
86. Pau, G., Fuchs, F., Sklyar, O., Boutros, M., and Huber, W. (2010). EBImage–an R package for image processing with applications to cellular phenotypes. Bioinformatics *26*, 979–981. https://doi.org/10.1093/BIOINFORMATICS/BTQ046.
87. Kuppe, C., Ramirez Flores, R.O., Li, Z., Hayat, S., Levinson, R.T., Liao, X., Hannani, M.T., Tanevski, J., Wünnemann, F., Nagai, J.S., et al. (2022). Spatial multi-omic map of human myocardial infarction. Nature *608*, 766. https://doi.org/10.1038/s41586-022-05060-x.
88. Korsunsky, I., Millard, N., Fan, J., Slowikowski, K., Zhang, F., Wei, K., Baglaenko, Y., Brenner, M., Loh, P.R., and Raychaudhuri, S. (2019). Fast, sensitive and accurate integration of single-cell data with Harmony. Nat. Methods *16*, 1289–1296. https://doi.org/10.1038/s41592-019-0619-0.
89. Blanco-Carmona, E. (2022). Generating publication ready visualizations for Single Cell transcriptomics using SCpubr. Preprint at bioRxiv. https://doi.org/10.1101/2022.02.28.482303.

STAR★METHODS

KEY RESOURCES TABLE

REAGENT or RESOURCE	SOURCE	IDENTIFIER
Antibodies		
Anti-Laminin (1:200 for IF)	Sigma-Aldrich	Cat# L9393; RRID: AB_477163
Anti-Col1A (COL-1) (1:200 for IF)	Santa Cruz Biotechnology	Cat# sc-59772; RRID: AB_1121787
Anti-Synaptophysin Polyclonal Antibody (1:300 for IF)	Invitrogen	Cat # PA1-1043; RRID: AB_2199026
Anti-Myosin (MF20) (1:20 for IF)	DSHB	N/A
Myosin heavy chain, Type 2B BF-F3 (1:50 for IF)	DSHB	N/A
Myosin heavy chain, Type 2A 2F7 (1:20 for IF)	DSHB	N/A
Myosin heavy chain, Type 1 BA-D5 (1:20 for IF)	DSHB	N/A
Anti-Caveolin-3 (1:1000 for IF)	BD Transduction Laboratories	Cat# 610420; RRID: AB_397800
Goat anti-Mouse IgM Alexa Fluor 555 (1:200 for IF)	Invitrogen	Cat# A-21426; RRID: AB_2535847
Goat anti-Mouse IgG(H + L) Alexa Fluor 647 (1:300 for IF)	Invitrogen	Cat# A-21235; RRID: AB_2535804
Goat anti-Mouse IgG(H + L) Alexa Fluor 488 (1:300 for IF)	Invitrogen	Cat# A-11001; RRID: AB_2534069
Goat anti-Rabbit IgG(H + L) Alexa Fluor 647 (1:300 for IF)	Invitrogen	Cat# A-21244; RRID: AB_2535812
Goat anti-Rabbit IgG(H + L) Alexa Fluor 594 (1:300 for IF)	Invitrogen	Cat# A-11012; RRID: AB_2534079
Chemicals, peptides, and recombinant proteins		
Tissue-Tek OCT Compound	VWR	Cat# 361603E
2-Methylbutane	Sigma Aldrich	Cat# 27, 034-2
SSC Buffer 20x Concentration	Millipore Sigma	Cat# S6639L
Triton X-100 Solution, ~10% in H_2O	Sigma Aldrich	Cat# 93443-100ML
RiboLock RNase Inhibitor	Thermo Fisher	Cat# EO0382
Ribonucleoside Vanadyl Complex (200 mM)	Sigma Aldrich	Cat# R3380
Tris 1M, pH 7.0, RNase-free	Thermo Fisher Scientific	Cat# AM9850G
Low TE Buffer (10 mM Tris-HCl pH 8.0, 0.1 mM EDTA)	Thermo Fisher Scientific	Cat # 12090-015
Hydrochloric Acid Solution, 0.1N	Fisher Chemical	Cat# SA54-1
Methanol, for HPLC, ≥99.9%	Millipore Sigma	Cat# 34860
Qiagen Buffer EB	Qiagen	Cat#19086
DAPI	Invitrogen- Thermo Fisher Scientific	Cat# D1306
alpha-bungarotoxin, Alexa Fluor 488 (1:200 for IF)	Invitrogen- Thermo Fisher Scientific	Cat# B13422
alpha-bungarotoxin, Alexa Fluor 594 (1:200 for IF)	Invitrogen- Thermo Fisher Scientific	Cat# B13423
Zoletil 50	Virbac	N/A
Rompun	BAYER	N/A
β-Mercaptoethoethanol	Sigma Aldrich	Cat# M3148
UltraPure™ DNase/RNase-Free Distilled Water	Life Technologies	Cat# 10977-035
Ethanol	Sigma Aldrich	Cat# 02851
NADH (disodium salt, approx 100% grade)	Roche	Cat# 10107735001
NBT (4-Nitro blue tetrazolium chloride)	Roche	Cat# 11087479001
Albumin (BSA) Fraction V (pH 7.0)	PanReac AppliChem	Cat# A1391,0100
PBS tablets pH 7.4	PanReac AppliChem	Cat# A9201,0010
Eukitt Quick mounting medium	Sigma Aldrich	Cat# 03989
Sardomozide dihydrochloride	Medchem Express	HY-13746B-10mg
Eflornithine hydrochloride hydrate (DFMO)	Medchem Express	HY-B0744B-1g
DMEM High W/Glutamax	Life Technologies	Cat# 61955059
Fetal Bovin Serum	Life Technologies	Cat# 10270106

(*Continued on next page*)

Continued

REAGENT or RESOURCE	SOURCE	IDENTIFIER
Horse serum	Gibco	Cat# 26050088
PBS w/o calcium chloride and magnesium chloride	Sigma Aldrich	Cat# D8537
Penicillin-Streptomycin	EuroClone	Cat# ECB3001D
SuperFrost® Plus adhesive microscope slides	Thermo Fisher Scientific	Cat# 9161155
Critical commercial assays		
KAPA SYBR FAST qPCR Master Mix (2X)	KAPA Biosystems	Cat# KK4600
2x Fast Q-PCR Master Mix (SYBR, ROX)	SMOBIO	Cat# TQ1211
RNeasy mini-kits	Qiagen	Cat# 74106
PrimeScriptTM RT Reagent Kit with gDNA Eraser (Perfect Real Time)	Takara	Cat# RR047A
Deposited data		
Healthy and SOD1^{G93A} Spatial Transcriptomic Dataset	This Paper	GEO: GSE271011
Healthy and denervated Spatial Transcriptomic Dataset	This Paper and D'Ercole et al.[26]	GEO: GSE281403
SOD1^{G93A} TA muscle (RNAseq Dataset)	Scaricamazza et al.[10]	https://www.ncbi.nlm.nih.gov/Traces/study/?acc=PRJNA623256
Original code to reproduce analysis and figures	This Paper	https://doi.org/10.5281/zenodo.14243515
C2C12 treated with Sardomozide (RNAseq Dataset)	This Paper	GEO: GSE271039
Experimental models: Cell lines		
C2.C12	ATCC	Cat# CRL-1772
Experimental models: Organisms/strains		
Mouse Model: C57BL/6J	https://www.jax.org/strain/000664	Cat# 000664
Mouse Model: B6SJL-Tg(SOD1*G93A)1Gur/J	https://www.jax.org/strain/002726#	Cat# 002726
Oligonucleotides		
Primer: ActB FW CACTGTCGAGTCGCGTCC	This paper	N/A
Primer: ActB RV TCATCCATGGCGAACTGGTG	This paper	N/A
Primer: Amd 1/2 FW TGCAATTTTCCCAAATGGAGCA	This paper	N/A
Primer: Amd 1/2 RV CTGCTGGGTCAAGCTCACTC	This paper	N/A
Primer: Amd 2 FW GCTTTCGTCCCCATTAGATGC	This paper	N/A
Primer: Amd 2 RV CCCTAGAAAGTGGAGGTAACTG	This paper	N/A
Primer: Odc1 FW GCTGTGTCATGGAGAGACCC	This paper	N/A
Primer: Odc1 RV CTCTCCTCTGTGCGG	This paper	N/A
Primer: Smox FW AGCTCCAAGACAGCGCATAG	This paper	N/A
Primer: Smox RV GGTCCAGGGATTGTTCTGGG	This paper	N/A
Primer: Srm FW GTAGCAAAAACCCGAGCACC	This paper	N/A
Primer: Srm RV GTGAACTCGGGCAGTACGAA	This paper	N/A
Primer: Sms FW TGCTGAATTTCCCTCTTGGCT	This paper	N/A
Primer: Sms RV GGCAAAGCTGCCATTCTTGT	This paper	N/A
Primer: Sat1 FW TGACCCATGGATTGGCAAGT	This paper	N/A
Primer: Sat1 RV CAGCGACACTTCATGGCAAC	This paper	N/A
Primer: Paox FW CAGAAGCTCTGCAGCCACC	This paper	N/A
Primer: Paox RV CTCCACTACACCACCGAAGC	This paper	N/A
Primer: Atp13a3 FW ATGGCACCGGATCAGAAGAC	This paper	N/A
Primer: Atp13a3 RV TGCCCTCTTCAAAGCACCAC	This paper	N/A
Primer: Etv5 FW AGATGCTGTGTCATTTCAGGAGT	This paper	N/A
Primer: Etv5 RV TGGTGCTTCCAAAGTCTCCG	This paper	N/A
Primer: Colq FW CAATCTCAGCAGCCCTTCCT	This paper	N/A
Primer: Colq RV GGGCATGAGTAGGCAGCAT	This paper	N/A

(*Continued on next page*)

Continued

REAGENT or RESOURCE	SOURCE	IDENTIFIER
Primer: Chrne FW GATGCTGTGAACTTTGTGGCT	This paper	N/A
Primer: Chrne RV CCCAGTCGGACAGTTCCTCTC	This paper	N/A
Primer: Ache FW GACCAATTTTGCCCGCACAG	This paper	N/A
Primer: Ache RV CAGAGTATCGGTGGCGCTG	This paper	N/A
Primer: Itga4 FW CCAGGCATTCATGCGGAAAG	This paper	N/A
Primer: Itga4 RV ATGCCCAAGGTGGTATGTGG	This paper	N/A
Primer: Gabrb2 FW GCACGGGTTGCATTAGGAAT	This paper	N/A
Primer: Gabrb2 RV TAGGGAGAGTTTCCCGGAGG	This paper	N/A
Primer: Grip1 FW GAGCGAGCCAGCGAGTA	This paper	N/A
Primer: Grip1 RV GTGTAGGGACTCTCATCTCTCT	This paper	N/A
Primer: Sema 6c FW CGGATCTCGGAGCAAGTACC	This paper	N/A
Primer: Sema 6c RV CTCATCAGGCTGCCTCTGG	This paper	N/A
Primer: Nr4a3 FW TACGCCACGCAGACTTATGG	This paper	N/A
Primer: Nr4a3 RV TGGTCAGCTTGGTGTAGTCG	This paper	N/A
Primer: Ppargc1a FW GTCAACAGCAAAAGCCACAA	This paper	N/A
Primer: Ppargc1a RV TCTGGGGTCAGAGGAAGAGA	This paper	N/A
Primer: Mtfp1 FW AATGGACCACCACCACACTT	This paper	N/A
Primer: Mtfp1 RV AAGTCCACTGACCTGTCGAT	This paper	N/A
Primer: Ankrd1 FW GGATGTGCCGAGGTTTCTGA	This paper	N/A
Primer: Ankrd1 RV AGTGCCGTCCGTTTATACTCA	This paper	N/A
Primer: Myot FW CCCCTCTGAGCTAAGGAAACAA	This paper	N/A
Primer: Myot RV TGCAGCAAGTCAGAAGCAAC	This paper	N/A
Primer: Mylk4 FW AGTCCTGCAGTCCCTCTGAA	This paper	N/A
Primer: Mylk4 RV GCACTCCCTTCTCTTGACATCT	This paper	N/A
Primer: Sln FW CTCCTCTTCAGGAAGTGAAGACA	This paper	N/A
Primer: Sln RV GCTCCTGAGTAGACCTCTCCAT	This paper	N/A
Primer: Myog FW GTCCCAACCCAGGAGATCAT	This paper	N/A
Primer: Myog RV GCTGTCCACGATGGACGTAA	This paper	N/A
Primer: Hdac4 FW CAGACAGCAAGCCCTCCTAC	This paper	N/A
Primer: Hdac4 RV AGACCTGTGGTGAACCTTGG	This paper	N/A
Primer: Mb FW CTGTTTAAGACTCACCCTGAGAC	This paper	N/A
Primer: Mb RV GGTGCAACCATGCTTCTTCA	This paper	N/A
Primer: Gadd45a FW TGGTGACGAACCCACATTCA	This paper	N/A
Primer: Gadd45a RV TCCATGTAGCGACTTTCCCG	This paper	N/A
Primer: mt-Nd5 FW ACCCAATCAAACGCCTAGCA	This paper	N/A
Primer: mt-Nd5 RV AGGACTGGAATGCTGGTTGG	This paper	N/A
Primer: Ndufa5 FW CGGGCTTGCTGAAAAAGACA	This paper	N/A
Primer: Ndufa5 RV TAACATCTGGCTCCTCGTGTG	This paper	N/A
Primer: Cox7a1 FW GCCTAACCTAAACATGCCAGGA	This paper	N/A
Primer: Cox7a1 RV GGTCATTGTCGGCCTGGAAG	This paper	N/A
Primer: Ndufa4 FW AGAAGCATCCCAGCTTGATTCC	This paper	N/A
Primer: Ndufa4 RV TAAACAGTGCCAAGCGCATC	This paper	N/A
Primer: Ndufa6 FW AGTACCTCGGTGAAGCCCAT	This paper	N/A
Primer: Ndufa6 RV TGCATTAAGTGCACGGTGTTC	This paper	N/A
Primer: Trim63 FW ACCACAGAGGGTAAAGAAGAACA	This paper	N/A
Primer: Trim63 RV GCAGAGAGAAGACACACTTCCC	This paper	N/A
Primer: Fbxo32 FW CTCAGAGAGGCAGATTCGCA	This paper	N/A
Primer: Fbxo32 RV GGTGACCCCATACTGCTCTC	This paper	N/A

(*Continued on next page*)

Continued

REAGENT or RESOURCE	SOURCE	IDENTIFIER
Software and algorithms		
GraphPad Prism 10	–	http://www.graphpad.com
ImageJ	Schneider et al.[73]	https://imagej.nih.gov/ij/
Space Ranger 3.0.0	10X Genomics	https://support.10xgenomics.com/spatial-gene-expression/software/pipelines/1.1/what-is-space-ranger
Seurat 5.1.0	Hao and Hao et al.[74]	https://github.com/satijalab/seurat
dplyr 1.1.4	Wickham H et al.[75]	https://CRAN.R-project.org/package=dplyr
cowplot 1.1.3	Wilke et al.[76]	https://cloud.r-project.org/package=cowplot
ggplot2 3.5.1	Wickham et al.[77]	https://ggplot2.tidyverse.org
ggrepel 0.9.6	Slowikowski et al.[78]	https://ggrepel.slowkow.com/
Sctransform 0.3.3	Hafemeister & Satija[79]	https://cran.r-project.org/web/packages/sctransform/index.html
Patchwork 1.3.0	Pedersen[80]	https://cran.r-project.org/web/packages/patchwork/index.html
Viridis 0.6.5	Garnier et al.[81]	https://sjmgarnier.github.io/viridis/
gprofiler2 0.2.1	Peterson et al.[82]	https://biit.cs.ut.ee/gprofiler/page/r
clusterProfiler 4.10.1	Wu et al.[83]	https://bioconductor.org/packages/release/bioc/html/clusterProfiler.html
Org.Mm.e.g.,.db 3.18.0	Carlson[84]	https://bioconductor.org/packages/release/data/annotation/html/org.Mm.eg.db.html
eulerr 7.0.2	Larsson[85]	https://cran.r-project.org/web/packages/eulerr/index.html
EBImage_4.44.0	Pau et al.[86]	https://bioconductor.org/packages/release/bioc/html/EBImage.html
QuantStudio 7 Flex	Appliedbiosystems, Thermo Scientific	N/A
NanoDrop ONE^{c} spectrophotometer	Thermo Scientific	ND-ONE-W
LSM 900 with Airyscan2	Zeiss	N/A

EXPERIMENTAL MODEL AND STUDY PARTICIPANT DETAILS

Mouse lines

C57BL/6J and SOD1^{G93A} mice (B6.Cg-Tg(SOD1 G93A)1Gur/J) were provided by the Jackson Laboratory (Bar Harbor, USA). To obtain the offspring, transgenic hemizygous SOD1^{G93A} male mice were crossbred with female C57BL/6J; the generated animals were genotyped by PCR with hSOD1 oligos (Fw: 5′-CATCAGCCCTAATCCATCTGA-3′; Rev: 5′-CGCGACTAACAAT CAAAGTGA-3′) and IL2 as internal control (Fw: 5′-TAGGCCACAGAATTGAAAGATCT-3′; Rev: 5′-GTAGGTGGAAATTCTAGCAT CATC C-3′).

All mice were maintained in a pathogen-free animal facility under standard 12h light/12h dark cycle at 21°C with access to red house and to standard chow and water *ad libitum*. Male mice were used for *in vivo* experiments. All experiments in this study were performed in accordance with protocols approved by Italian Ministry of Health, Sapienza University of Rome (Rome) and IRCCS Santa Lucia Foundation. The study is compliant with all relevant ethical regulations regarding animal research and in the respect of the principles of the 3Rs (Replacement, Reduction and Refinement).

DFMO treatment

0.2% of difluoromethylornithine (DFMO) (Medchem Express, HY-B0744B) was dissolved in drinking water and administered to male SOD1^{G93A} mice from 50 days to 75 days of age. During the period of the treatment, weight and muscular strength were assessed twice a week to evaluate the progression of the disease. Muscular strength was measured with a dynamometric evaluation of grip strength by grid net, which provide an index of neuromuscular function expressed as maximal strength of muscles

(32981. https://doi.org/10.3402/pba.v6.32981). As previously described, the test consisted of three attempts for each mouse, spaced out with 1 min for rest; the mean of the three examinations was normalized to the weight of each respective mouse (https://doi.org/10.1111/bph.15738; https://doi.org/10.3389/fphar.2024.1360099). The test was carried out by the same operator to minimize experimental variability.

Sardomozide treatment

Male C57BL/6J mice received intraperitoneal injections of 2 mg/kg sardomozide dihydrochloride (Sardo) dissolved in PBS (vehicle) three times a week for a fortnight (15 days). Control littermates were injected with PBS following the same protocol. During the treatment period, the body weight of the mice was assessed three times a week. At the end of the treatment, the mice were sacrificed, and their muscles were harvested for histological analysis.

METHOD DETAILS

Denervation

Unilateral hindlimb denervation was performed by cutting the sciatic nerve under anesthesia by intraperitoneal injection of 40 mg/kg Zoletil (zolazepam + tiletamine) and 10 mg/kg Rompun (xylazine). After exposing sciatic nerve by cutting the skin near the knee, a 5mm segment of the nerve was removed to prevent regeneration. After surgery, the incision was closed using 3M Vetbond Tissue Adhesive. The mice were monitored until the date of sacrifice, and successful denervation was confirmed with a grip strength test.

Spatial Transcriptomics library preparation and analysis

TA plus EDL muscles were collected from adult C57BL/6J (age range 2.5–5 months old – $n = 2$) and SOD1^{G93A} mice at 75 days ($n = 3$) and 150 days ($n = 2$). Muscles were embedded in OCT (VWR), then frozen in liquid nitrogen for 15 s and stored at -80°C. Spatially tagged cDNA libraries were built using a Visium Spatial Gene Expression 3′ Library Construction v1 Kit (10x Genomics, PN-1000187; Pleasanton, CA). The optimal tissue permeabilization time for 10 μm-thick sections was determined to be 15 min using a 10x Genomics Visium Tissue Optimization Kit (PN-1000193). Immunofluorescence-stained tissue sections were imaged using a Zeiss confocal microscope (LSM 900 with Airyscan2) with a mechanical plate.

The primary probes used for immunofluorescence were rabbit anti-laminin (1:200), mouse anti-collagen-1 (1:200), and BTX 594 (1:200). Antibody binding specificity was revealed using secondary antibodies coupled to Alexa Fluor 488 or 647. Libraries were generated from cDNA following the manufacturer's instructions and checked with both a Qubit 2.0 Fluorometer (Invitrogen, Carlsbad, CA) and an Agilent Bioanalyzer DNA assay (Agilent Technologies, Santa Clara, CA). Libraries were then sequenced in paired-end 150 bp mode on a NovaSeq 6000 system (Illumina, San Diego, CA).

Frames around the capture area on the Visium slide were aligned manually, and spots distributed across the tissue were selected using Loupe Browser v7.0.0 software (10x Genomics). The sequencing data were then aligned to the mouse reference genome (mm10) using the Space Ranger v2.1.1 pipeline (10x Genomics) to generate a feature-by-spot-barcode expression matrix. Analysis was performed using Seurat v5 (scripts to reproduce the workflow and figures are available on Zenodo and attached as supplemental information - see data and code availability). Integration was performed as in Kuppe at al.[87] with minor modifications. Briefly, each section was loaded using the Load10X_Spatial () function and preprocessed separately by applying sctransform normalization. After this initial step, sections were integrated using both IntegrateData () and Harmony package.[88] For IntegrateData () normalization method parameter was set to ''SCT''. UMAP and clustering were performed on Harmony adjusted embeddings. Cluster markers were identified using the ''FindAllMarkers'' function with the following parameters: only.pos = TRUE, min.pct = 0.25, and logfc.threshold = 0.25. Average expression data were obtained using ''AverageExpression'' functions. When displaying gene expression for the whole dataset across the different images, maximum value for scale limit was set to 99th percentile of total expression across samples to harmonize scales and improve visualization. SCpubr package[89] was used to generate Feature and Dim plot graphs. GO analysis was performed using clusterProfiler v4.12.0 pacakge[83].

RNA analysis by quantitative PCR

Total RNA was extracted from frozen muscle tissue using Tri-reagent (Zymo Research) according to the manufacturer's instructions. RNA quantification was performed using a NanoDrop ONE^{c} spectrophotometer (Thermo Scientific). First-strand cDNA was synthesized from the extracted RNA using a PrimeScript RT Reagent Kit with gDNA Eraser (Takara) following the manufacturer's protocols. mRNA expression levels were determined by quantitative real-time PCR via QuantStudio 7 Flex (Applied Biosystems, Thermo Scientific) system using the ExcelTaq 2X Fast Q-PCR Master Mix (SYBR, ROX) (Smobio). Relative gene expression was calculated using the $2^{-\Delta\Delta CT}$ method and normalized to the expression of the housekeeping gene actin beta (ActB).

RNA-sequencing

Total RNA from C2C12 myotubes was extracted using Qiagen RNeasy mini kits following the manufacturer's protocol. RNA was sent to The Institute of Applied Genomics (IGA) of Udine (IT) (https://appliedgenomics.org/it/) for sequencing. The libraries for sequencing were prepared using the Illumina kit and sequenced with Illumina NovaSeq (paired end 150pb). For each biological sample three independent experiments were carried out for the isolation of RNA. Base calling, demultiplexing and adapter masking were carried out

with BCL Converter v3.9.3. Low quality bases and adapters were then removed by ERNE software. Subsequently, reads were aligned to transcriptome GRCm38 (mm10) using STAR with default parameters. The software Stringtie, with default parameters, was used to assemble and quantify full-length transcripts representing multiple spliced variants for each gene locus. RSeqQC was used for the Quality control of read distribution along transcripts. Count tables were generated in R using the package DESeq2. Differential expression of genes was conducted using DESeq2 with default options. Genes were considered differentially expressed if the adjusted *p*-value was<0.05. Gene Ontology was performed using the function gseGO, comprised in the R package clusterProfiler v4.12.0.[83] Significant gene lists (pvalue_Adj <0.05) were extracted from DESeq2 differential expression tables and processed with the following non-default parameters: ont BP, nPermSimple 10000, minGSSize 3, maxGSSize 800, OrgDb org.Mm.e.g.,.db, pAdjustMethod none.

Histological staining

For immunofluorescence staining, 10μm muscle cryosections were permeabilized with 100% acetone for 1 min at room temperature, followed by blocking for 1 h with a blocking solution containing 4% BSA (MilliporeSigma, A7030-100G) in PBS 1X. For myosin immunostaining, cryosections were not fixed but immediately incubated with a solution of 10% Goat Serum in PBS for 10 min. Primary antibodies were diluted in blocking solution, with incubation performed overnight at 4°C or, for myosin staining, for 30 min at room temperature. Antibody binding specificity was revealed using secondary antibodies coupled to Alexa Fluor 488, 647, 594 or 555. Incubation with secondary antibody was carried out at room temperature for 1 h. The primary antibodies used for immunofluorescence included: anti-synaptophysin (1:300, Invitrogen, PA1-1043), anti-caveolin-3 (1:1000, BD Transduction Laboratories, 610420), anti-laminin (1:300, MilliporeSigma, L9393) and mouse monoclonal antibodies from the Development Studies Hybridoma Bank (DSHB, Iowa, USA) for MyHC-2A (2F7, 1:20 for IF), MyHC-2B (BF-F3, 1:50 for IF) and MyHC-1 (BA-D5, 1:20 for IF). AChRs were revealed using fluorescently labeled BTX (1:300 Alexa 594, Invitrogen, B13423 or Alexa 488, Invitrogen, B13422). After immunostaining, sections were incubated with DAPI (Thermo Fisher Scientific, D1306) in PBS for 5 min for nuclear staining, washed in PBS, and mounted with glycerol (3:1 in PBS). Transverse sections were visualized on a Zeiss confocal microscope and edited using ImageJ software. Muscle fibers CSA analyses were performed using ImageJ software. All reported images are representative of all examined fields.

For NADH-TR staining, sections were placed in a buffer solution (0.1 M Tris HCl, pH 7.5, in ddH_2O) for 5 min, then stained with an NADH solution (2 mg of NADH and 4 mg of NBT in 0.1 M Tris HCl, pH 7.5, in ddH_2O) for 1 h at 37° in the dark. After removing the dye, muscle sections were further dried in ethanol with gradually increasing concentrations and fixed in 100% toluene before being mounted with EUKITT mounting medium (Sigma–Aldrich). The sections were imaged using a Zeiss Imager A2.

C2C12 culture

C2C12 myogenic cells were obtained from ATCC and cultured in 96-well plates in growth medium (DMEM [-Pyruvate], Gibco, 61965-026; supplemented with 10% of FBS and 1% of penicillin/streptomycin). Myogenic differentiation was induced by shifting the cells to differentiation medium (DMEM [-Pyruvate] complemented with 2% horse serum and 1% penicillin/streptomycin). Fully differentiated C2C12 myotubes were treated with Sardomozide dihydrochloride (Medchem Express HY-13746B) at concentrations of 10μM or 100μM for 72h in differentiation medium. To analyze the morphology of the myotubes, they were fixed in 4% PFA (MilliporeSigma, P6148) for 10 min at room temperature and then permeabilized with 0.1% Triton X-100 for another 10 min. The myotubes were then blocked for 1 h with a solution containing 4% BSA (MilliporeSigma, A7030-100G) in PBS 1X. The primary antibody (anti-Myosin; 1:20, DSHB, MF20) immunostaining was performed overnight at 4°C, and antibody binding specificity was revealed using a secondary antibody coupled to Alexa Fluor 488 (goat anti-rabbit Alexa Fluor 488, A32731). Nuclear staining was performed by incubating cells with DAPI (Thermo Fisher Scientific, D1306) in PBS for 5 min. Images were acquired using a Zeiss confocal microscope. The morphological analysis of myotubes size was conducted using ImageJ software, with three measurements per myotube used for the diameters analysis. The mean value of these measurements was used for the subsequent statistical analysis. The reported figures are representative of all the examined fields.

Polyamine analysis

Polyamine content was determined by gas chromatography-mass spectrometry (GC-MS) and the values were normalized by muscle weight. Muscles pulverized in liquid nitrogen were resuspended in 0.2 M $HClO_4$ and homogenized in an ice-bath using an ultra-turrax T8 blender. The homogenized tissue was centrifuged at 13,000× g for 15 min at 4°C; 0.5 mL of supernatant was spiked with internal standard 1,6-diaminohexane and adjusted to pH $\geq$ 12 with 0.5 mL of 5 M NaOH. The samples were then subjected to sequential N-ethoxycarbonylation and N-pentafluoropropionylation. GC-MS analyses were performed with an Agilent 7890B gas chromatograph coupled to a 5977B quadrupole mass selective detector (Agilent Technologies, Palo Alto, CA). Chromatographic separations were carried out with an Agilent HP-5ms fused-silica capillary column. Mass spectrometric analysis was performed simultaneously in TIC (mass range scan from m/z 50 to 800 at a rate of 0.42 scans s–1) and SIM mode (put, m/z 405; spd, m/z 580, spm, m/z 709).

Figure design

The graphical abstract, Figures 1A, 3C, 6A, 6C, 6G, 7A, and S3C were created with BioRender (https://biorender.com/), license to Dr. Madaro Luca.

QUANTIFICATION AND STATISTICAL ANALYSIS

Statistical analysis

Data are presented as the mean ± SEM. Comparisons were conducted using Student's t test, assuming a two-tailed distribution, or the two-way ANOVA multiple-comparison test, with significance defined as $p < 0.05$ (*), $p < 0.01$ (**), $p < 0.001$ (***) or $p < 0.0001$ (****). The number of biological replicates for each experiment is indicated in the corresponding figure legend. Histological and immunofluorescence images are representative of at least 3 different experiments/animals.